J. Mech. Phys. Solids 151 (2021) 104400

Contents lists available at ScienceDirect

Journal of the Mechanics and Physics of Solids

journal homepage: www.elsevier.com/locate/jmps

Mechanics of encapsulated three-dimensional structures for simultaneous sensing of pressure and shear stress

Xuebo Yuan [a,b], Sang Min Won [c], Mengdi Han [c], Youshan Wang [a], John A. Rogers [c,d,e,f], Yonggang Huang [b,c,d,e], Heling Wang [b,d,e,*]

[a] Center for Composite Materials and Structures, Harbin Institute of Technology, Harbin 150080, China
[b] Department of Civil and Environmental Engineering, Northwestern University, Evanston IL 60208, USA
[c] Center for Bio-Integrated Electronics, Northwestern University, Evanston IL 60208, USA
[d] Department of Mechanical Engineering, Northwestern University, Evanston IL 60208, USA
[e] Department of Materials Science and Engineering, Northwestern University, Evanston IL 60208, USA
[f] Departments of Biomedical Engineering, Chemistry, Electrical Engineering and Computer Science, Neurological Surgery, Simpson Querrey Institute for BioNanotechnology, McCormick School of Engineering and Feinberg School of Medicine, Northwestern University, Evanston IL 60208, USA

ARTICLE INFO

Keywords:
Simultaneous pressure/shear sensor
Mechanics-guided, deterministic 3D assembly
Soft encapsulation
Analytic model

ABSTRACT

Flexible, large-area tactile sensors capable of simultaneously measuring in real time both the normal pressure and the tangential shear stress have many important applications, including those in artificial skin for uses in robotics, medicine and rehabilitation. Previously reported sensors exhibit responses to pressure and shear stress that are coupled, mainly due to non-linearities, in ways that can be difficult to separate. A recently developed sensor based on techniques in mechanics-guided, deterministic three-dimensional (3D) assembly provides a route to decouple these responses such that the pressure and the shear stress can be determined explicitly and linearly from the change in resistance of multiple strain gauges integrated at carefully selected locations on the 3D structure. A clear understanding of the mechanics of this 3D structure-based sensor is essential for its optimization and application. Here analytic models, validated by finite element analysis, are presented for the deformation of such structures under pressure and shear stress. Analytic solutions in concise forms are derived for a buckled wavy ribbon encapsulated in a soft elastomer, which reveal the effect of the geometry and material parameters on the sensitivity, therefore establishing design guidelines for these devices.

1. Introduction

Stretchable electronic systems that integrate high performance materials and functional components serve as the technology foundations for artificial skins that can mimic the mechanical properties and many of the sensory capabilities of human skin (Rogers et al., 2010; Chortos et al., 2016; Someya et al., 2016; Liu et al., 2017; Ma et al., 2018; Yao et al., 2018; Chung et al., 2019; Kim et al., 2019; Yang et al., 2019; Yu et al., 2019; Ma et al., 2020; Xie et al., 2020), including responsiveness to multiple external stimuli such as lateral strain (Yao and Zhu, 2014; Jang et al., 2015; Ma et al., 2016; Ma and Zhang, 2016; Pan et al., 2017; Chen et al., 2018; Zhu et al., 2019), bending strain (Lu et al., 2012; Wang et al., 2016a; Chen et al., 2017), pressure (Lipomi et al., 2011; Yao and Zhu, 2014; Bae

* Corresponding author.
E-mail address: helingwang1@gmail.com (H. Wang).

https://doi.org/10.1016/j.jmps.2021.104400
Received 20 October 2020; Received in revised form 28 February 2021; Accepted 13 March 2021
Available online 15 March 2021

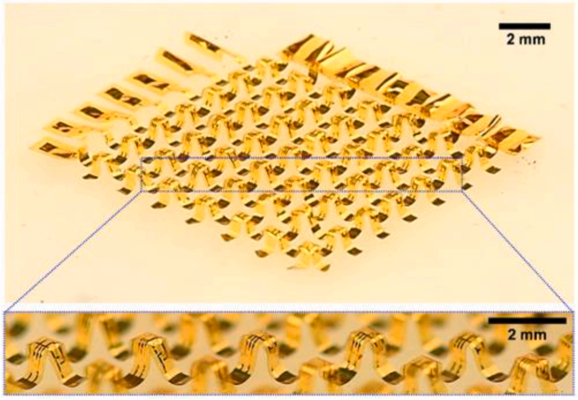

Fig. 1. An experimental image of a 7×7 3D sensor array fabricated by mechanics-guided, deterministic 3D assembly and encapsulated in PDMS elastomer. Source: Won et al. (2019), reprinted with permission of American Chemical Society, copyright (2019).

et al., 2018; Wu et al., 2018), shear force (Mu et al., 2018; Yang et al., 2018), vibration (Kang et al., 2014; Ha et al., 2019; Lee et al., 2019a) and temperature (Zhang et al., 2015a; Hong et al., 2016; Cui et al., 2019; Jeong et al., 2019). For many applications, it is important to differentiate and detect mechanical stimuli from both the normal direction (pressure) and the tangential direction (shear stress) (Scheibert et al., 2009; Dahiya et al., 2010; Heyneman and Cutkosky, 2016). For example, gentle grasping and dexterous manipulation of objects requires continuous tactile feedback on the pressure and shear stress, which occurs naturally and accurately across a human hand, but remains a challenge for robotic hands equipped with artificial skin (Birznieks et al., 2001; Crowder, 2006; Delmas et al., 2011; Yousef et al., 2011; Heyneman and Cutkosky, 2016; Yang et al., 2019). Although pressure and shear sensors are available based on various mechanisms including piezoresistive (Wang and Beebe, 2000; Gong et al., 2014; Park et al., 2014a; Park et al., 2014b; Kim et al., 2017), capacitive (Mannsfeld et al., 2010; Takei et al., 2010; Dobrzynska and Gijs, 2012; Sun et al., 2014; Boutry et al., 2018), piezoelectric (Ting et al., 2016; Yu et al., 2016), triboelectric (Lin et al., 2013; Dong et al., 2018; Ha et al., 2018), optical (Ohka et al., 2005; Al-Mai et al., 2017) and magnetic (Tomo et al., 2016; Wang et al., 2016b), and many materials including doped single crystalline silicon nanomembranes (Kim et al., 2014; Won et al., 2019), conductive nanomaterials (Park et al., 2014c; Kim et al., 2015; Ma et al., 2015; Park et al., 2015; Mu et al., 2018), conductive textiles (Viry et al., 2014; Ge et al., 2016), conductive elastomers (Charalambides and Bergbreiter, 2017; Park et al., 2018), piezoelectric polymers (Ting et al., 2016; Yu et al., 2016; Ha et al., 2018), ionic gels (Sun et al., 2014; Cho et al., 2017; Choi et al., 2019) and liquid metals (Vogt et al., 2013; Gao et al., 2017), it is difficult to simultaneously determine the pressure and shear stress when they are applied on the sensor at the same time, because one sensor output cannot determine two unknowns (pressure and shear stress). In addition, many of these pressure/shear stress sensors rely on microstructures and thin films of inorganic materials (Chu et al., 1996; Kane et al., 2000; Wang and Beebe, 2000) that are rigid and have low thresholds for fracture; they cannot be applied easily in wearable devices and human-machine interfaces. Some biomimetic sensors capable of differentiating the pressure and the shear stress adopt designs that mimic interlocked epidermal-dermal ridge microstructures (Pang et al., 2012; Park et al., 2014b; Park et al., 2018; Choi et al., 2019; Lee et al., 2019b), but they are unable to decouple the pressure and shear stress in real time, because they provide only one signal output. Multiple signal outputs have been realized in elastomer-based sensors (Lee et al., 2008; Cheng et al., 2010; Hu et al., 2011; Dobrzynska and Gijs, 2012; Viry et al., 2014; Charalambides and Bergbreiter, 2017; Boutry et al., 2018; Yang et al., 2018), but they are limited to small pressures and shear stresses (e.g., ~10 kPa in Boutry et al., 2018), beyond which the relations between the signal outputs and the pressure/shear stress become nonlinear and coupled such that the pressure and shear stress cannot be obtained analytically in terms of the signal outputs. Moreover, multi-component structures of elastomer-based sensors involve complexity in fabrication (Charalambides and Bergbreiter, 2017; Yang et al., 2019).

Recent work shows that mechanics-guided, deterministic three-dimensional (3D) assembly techniques (Xu et al., 2015; Zhang et al., 2015b; Yan et al., 2016; Ning et al., 2017; Fu et al., 2018; Ning et al., 2018; Xue et al., 2018; Han et al., 2019; Liu et al., 2019a; Won et al., 2019) can yield a multimodal sensor based on a table-like 3D structure encapsulated in soft elastomer (Fig. 1). With four integrated piezoresistive strain gauges (silicon-nanomembranes, Si-NMs for short), the sensor can detect both pressure and shear stress in real time (Won et al., 2019). A significant advantage of this sensor is that the changes in resistance of the Si-NMs are linearly proportional to the pressure (P) and shear stress (τ) in a large range, such that P and τ can be determined explicitly in terms of the signal outputs (i.e., resistance changes). Furthermore, the 3D assembly technique allows the formation of sensor arrays in efficient and low-cost manner, for spatially mapping the distribution of pressure and shear stress.

The sensitivity of such 3D structure-based sensors largely depends on the geometry and material parameters, such that an analytic model is essential for an optimized design. Past studies focused on the buckling of two-dimensional (2D) precursors on a pre-stretched substrate for a variety of geometries (Jiang et al., 2007a; Song et al., 2009; Wang et al., 2010; Su et al., 2012; Chen et al., 2016; Fan et al., 2018; Shi et al., 2018; Zhang et al., 2018; Li et al., 2019b; Liu et al., 2019a; Liu et al., 2019b; Luo et al., 2019), as well as deformation of the encapsulated 3D buckled structure subjected to in-plane stretching (Jiang et al., 2008; Kim et al., 2009; Wu et al., 2011; Li et al., 2019a). These models all assume that 1) shear stresses at the interface between the substrate/encapsulation and the

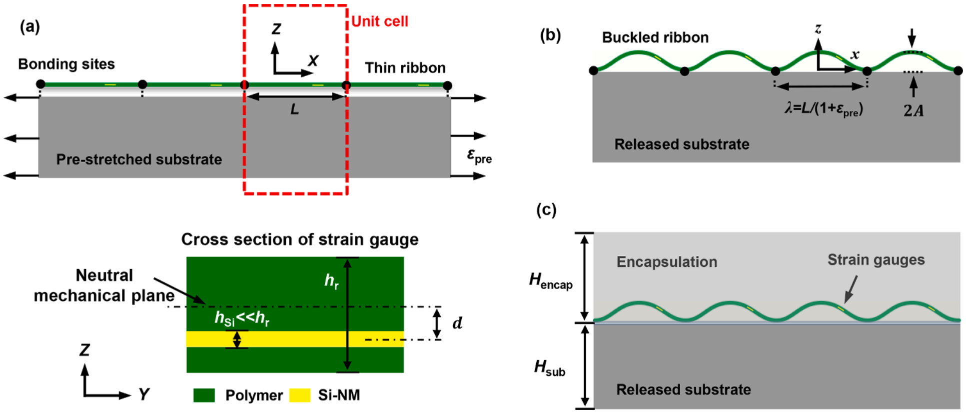

Fig. 2. Schematics of the process for fabricating the encapsulated wavy ribbon. (a) 2D precursor of a straight, strain-free ribbon with integrated strain gauges (Si-NMS), periodically bonded to the pre-strained elastomeric substrate. The Si-NMs are perfectly bonded with two polymer layers (e.g. polyimide). (b) After releasing the pre-strain, the ribbon transforms into a wavy configuration with wavelength λ and amplitude A. (c) The wavy ribbon is encapsulated with an elastomeric layer.

buckled structure vanish, which clearly does not hold when the shear stress and pressure are applied normal to the ribbon; and 2) encapsulation-ribbon and substrate-ribbon interfaces remain flat after buckling in order to calculate the elastic energy in the encapsulation and substrate, which is clearly inaccurate as the buckle amplitude of the ribbon can be orders of magnitude larger than the ribbon thickness.

Analytic models are developed in this paper for buckled wavy ribbon structures encapsulated in the soft elastomer subjected to remote pressure and shear stress. The analytic models do not involve the two assumptions 1) and 2) discussed above; specifically the assumption 1) of vanishing shear stress at the interface is replaced by the displacement continuity across the interface; and the assumption 2) of flat interfaces after buckling is no longer necessary as the wavy interfaces can be accurately accounted for. The strains (signal outputs) are obtained analytically in terms of both the pressure and shear stress, and they agree well with finite element analysis (FEA) without any parameter fitting. The analytic models are useful to optimize the sensor design for simultaneous determination of the pressure and shear stress.

2. Pressure sensing

2.1. The encapsulated wavy ribbon

Fig. 2a~c provides a schematic illustration of the mechanics-guided, deterministic 3D assembly technique. A stress-free, straight ribbon (elastic modulus E_r and thickness h_r) integrated with piezoresistive strain gauges (Si-NMs) is bonded to a pre-stretched (pre-strain ε_{pre}) substrate at patterned bonding sites to the substrate surface (Fig. 2a). The distance between two bonding sites on the pre-stretched substrate is L. Upon release of pre-stretch in the substrate, the straight ribbon buckles into a wavy shape (Fig. 2b), and the distance between two bonding sites becomes $\lambda = L/(1+\varepsilon_{pre})$. The buckle amplitude A has been determined as $A = \frac{L}{\pi}\sqrt{\frac{\varepsilon_{pre}}{1+\varepsilon_{pre}} - \varepsilon_c} \approx \frac{L}{\pi}\sqrt{\frac{\varepsilon_{pre}}{1+\varepsilon_{pre}}}$, where $\varepsilon_c = \frac{\pi^2 h_r^2}{3L^2}$ is the critical strain of buckling that is usually orders of magnitude smaller than ε_{pre} (Ko et al., 2009; Song et al., 2009; Wang et al., 2010). The dashed box in Fig. 2a shows a single unit cell (length L), consisting of the ribbon and substrate between two bonding sites, with periodic boundary conditions; and X is its coordinate along the ribbon. The bonding sites (as indicated by the black dots) are usually much smaller than the ribbon in length (Sun et al., 2006; Shi et al., 2018) such that their length is neglected. The ribbon is modeled as an elastic beam of thickness h_r. The Si-NM strain gauge is neglected in the analysis as it is much thinner (thickness h_{Si}~100 nm) than the ribbon (thickness h_r~5 μm). For small and moderate levels of pre-strain (e.g., ε_{pre}~20%), the out-of-plane displacement $w_0(X)$ and in-plane displacement $u_0(X)$ of the ribbon have been derived by an energy method (Ko et al., 2009; Song et al., 2009; Wang et al., 2010) as

$$w_0(X) = A\left[\cos\left(\frac{2\pi X}{L}\right)+1\right],\ u_0(X) = \frac{\pi A^2}{4L}\sin\left(\frac{4\pi X}{L}\right) - \frac{\varepsilon_{pre}}{1+\varepsilon_{pre}}X. \tag{1}$$

The membrane strain in the ribbon is simply $-\varepsilon_c$.

The buckled, wavy ribbon is then encapsulated by coating and thermally curing the prepolymer (Fig. 2c), which also completely fills the gaps between the wavy ribbon and the released substrate but does not induce further deformation in the ribbon (Sun et al., 2006; Jiang et al., 2008; Kim et al., 2009; Won et al., 2019). For the stress-free state of the encapsulation, the period (along the X direction) is $\lambda = L/(1+\varepsilon_{pre})$, and the coordinate in the same direction is $x = X + u_0(X)$. The out-of-plane displacement of the ribbon in Eq. (1) can be expressed in terms of x as (See Appendix A for details)

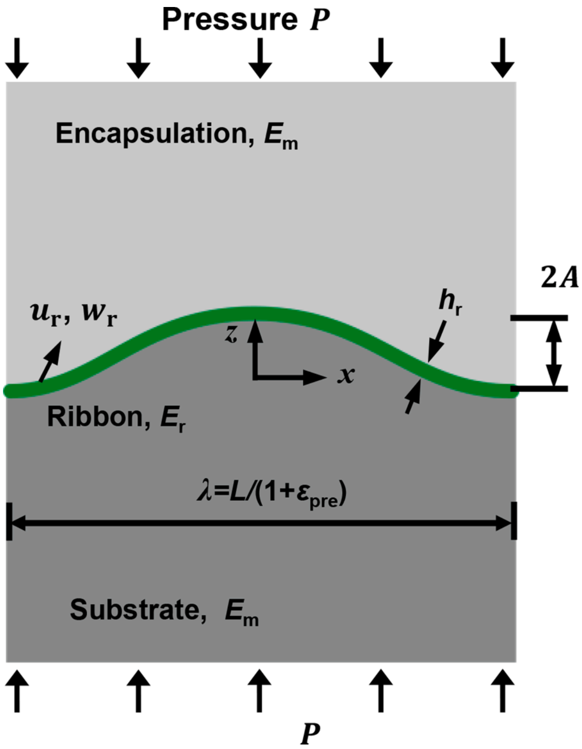

Fig. 3. Schematic of the model of a single unit cell under pressure.

$$w_0(x) = A\left[\cos\left(\frac{2\pi x}{\lambda}\right) + 1 + O\left(\frac{A^2}{L^2}\right)\right] \approx A\left[\cos\left(\frac{2\pi x}{\lambda}\right) + 1\right]. \tag{2}$$

Here $O\left(\frac{A^2}{L^2}\right)$ is neglected for small and moderate levels of pre-strain (Jiang et al., 2007b; Song et al., 2009) as $\frac{A^2}{L^2} = \frac{\varepsilon_{pre}}{\pi^2(1+\varepsilon_{pre})}$ which is ~2% for ε_{pre}~20%. Similarly, the in-plane displacement of the ribbon in Eq. (1) can be expressed in terms of x as (Jiang et al., 2007b)

$$u_0(x) = \frac{\pi A^2}{4\lambda}\left[\sin\left(\frac{4\pi x}{\lambda}\right) + O\left(\frac{A^2}{L^2}\right)\right] - \varepsilon_{pre}x \approx \frac{\pi A^2}{4\lambda}\sin\left(\frac{4\pi x}{\lambda}\right) - \varepsilon_{pre}x. \tag{3}$$

2.2. Encapsulation and substrate of the same material

As the pressure is applied on the top surface of the encapsulation (and bottom surface of the substrate, Fig. 3), the wavy ribbon deforms and the integrated piezoresistive strain gauge converts the mechanical signal (strain) into an electrical signal (resistance change). Most encapsulations and substrates are much thicker than the ribbons (Sun et al., 2006; Kim et al., 2009; Li et al., 2019; Won et al., 2019), therefore can be considered as semi-infinite. For simplicity the encapsulation and substrate are first assumed to have the same linear elastic modulus E_m, and the Poisson's ratio is $\upsilon_m = 0.5$ for incompressible elastomers. Fig. 3 shows a representative unit cell (periodic along the x- direction) of the encapsulated ribbon under pressure P. The wavy ribbon (modulus E_r and thickness h_r) is perfectly bonded with the elastomeric encapsulation and substrate such that the displacements are continuous across the ribbon/elastomer interfaces. The deformation is plane-stress in the x-z plane (Fig. 3), where z denotes the normal direction.

For the applied pressure much smaller than the elastic modulus of the encapsulation and substrate, $P << E_m$, the induced displacement is small and linearly elastic. FEA (see Appendix B for details) suggests that the out-of-plane displacement (z direction) of the wavy ribbon is well approximated by

$$w_r = \frac{P}{E_m}\alpha A\cos\left(\frac{2\pi x}{\lambda}\right), \tag{4}$$

where the dimensionless parameter α is to be determined and is independent of P. Because the encapsulation/ribbon and ribbon/substrate interfaces are wavy, the shear stresses at these interfaces are not zero even under the applied pressure, but they are opposite and approximately equal (for thin ribbons). Force equilibrium then requires the membrane strain to be uniform in the ribbon, which is confirmed by FEA (See Figs. B1a and B1b in Appendix B). This uniformity of the membrane strain $\varepsilon_{11} = \frac{d(u_0+u_r)}{dx} + \frac{1}{2}\left[\frac{d(w_0+w_r)}{dx}\right]^2$ gives the

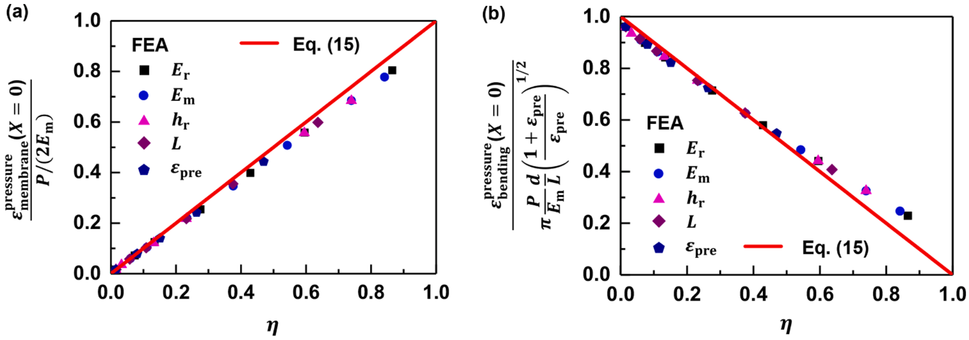

Fig. 4. The membrane strain $\varepsilon_{\text{membrane}}^{\text{pressure}}$ (a) and bending strain $\varepsilon_{\text{bending}}^{\text{pressure}}$ (b) in Si-NM located at $X=0$ (midpoint between two bonding sites) versus η, to validate the analytic model for semi-infinite encapsulation/substrate under pressure. The encapsulation and the substrate are of the same material. The Si-NM is located at the bottom of the ribbon with $d=0.5h_{\text{r}}$. The symbols denote FEA results for a range of material and geometric parameters as well as the pre-strain, and the lines denote analytic results.

in-plane displacement u_{r} as

$$u_{\text{r}}=\frac{P}{E_{\text{m}}}\left[\frac{\pi}{2}\alpha\frac{A^2}{\lambda}\sin\left(\frac{4\pi x}{\lambda}\right)+\beta x\right], \tag{5}$$

where only terms that are linearly proportional to P are kept, and the dimensionless parameter β is to be determined. The displacements in Eqs. (4) and (5) give the membrane energy and bending energy in the ribbon per period as (See Appendix C for details)

$$U_{\text{membrane}}^{\text{pressure}}=\frac{P^2}{E_{\text{m}}^2}E_{\text{r}}h_{\text{r}}\lambda\left(\frac{2\pi^4A^4}{\lambda^4}\alpha^2+\frac{2\pi^2A^2}{\lambda^2}\alpha\beta+\frac{1}{2}\beta^2\right), \tag{6}$$

$$U_{\text{bending}}^{\text{pressure}}=\frac{P^2}{E_{\text{m}}^2}E_{\text{r}}h_{\text{r}}^3\frac{\pi^4A^2}{3\lambda^3}\alpha^2. \tag{7}$$

The displacements u and w in the encapsulation and substrate satisfy the following equations of force equilibrium

$$\frac{\partial^2u}{\partial x^2}+\frac{1-\upsilon_{\text{m}}}{2}\frac{\partial^2u}{\partial z^2}+\frac{1+\upsilon_{\text{m}}}{2}\frac{\partial^2w}{\partial x\partial z}=0, \tag{8}$$

$$\frac{\partial^2w}{\partial z^2}+\frac{1-\upsilon_{\text{m}}}{2}\frac{\partial^2w}{\partial x^2}+\frac{1+\upsilon_{\text{m}}}{2}\frac{\partial^2u}{\partial x\partial z}=0. \tag{9}$$

The boundary conditions are the applied pressure P and zero shear remotely ($z=+\infty$ and $-\infty$ for the encapsulation and substrate, respectively), and continuity of displacements

$$u=u_{\text{r}},\ w=w_{\text{r}}\text{at } z=w_0(x) \tag{10}$$

at the interfaces with the wavy ribbon. Equation (10) is different from prior works Huang et al., 2005; Jiang et al., 2008; Wu et al., 2011) as it does not assume zero shear at the interfaces, and the interfaces are no longer flat. The solutions of Eqs. (8)–((10) for both the encapsulation and substrate are given in Appendix D. In principle, the strain energy $U_{\text{encap}}^{\text{pressure}}$ in the encapsulation and $U_{\text{sub}}^{\text{pressure}}$ in the substrate (per period) are quadratic functions of α and β. The external work due to pressure P is the $W_{\text{encap}}^{\text{pressure}}$ and $W_{\text{sub}}^{\text{pressure}}$ on the top surface of the encapsulation and bottom surface of the substrate, respectively, and they are linear with respect to α and β (see Appendix C for details). The total potential energy is

$$\Pi^{\text{pressure}}(\alpha,\beta)=U_{\text{membrane}}^{\text{pressure}}+U_{\text{bending}}^{\text{pressure}}+U_{\text{encap}}^{\text{pressure}}+U_{\text{sub}}^{\text{pressure}}-W_{\text{encap}}^{\text{pressure}}-W_{\text{sub}}^{\text{pressure}}, \tag{11}$$

where the first two terms of the right hand side are given in Eqs. (6) and (7). Minimization of the total potential energy gives α and β as

$$\alpha=-\frac{1-\eta}{4\varepsilon_{\text{pre}}\left(1+\varepsilon_{\text{pre}}\right)},\ \beta=\frac{1}{2}, \tag{12}$$

where η is given by

$$\eta=\frac{5\pi^3\frac{E_{\text{r}}h_{\text{r}}^3}{E_{\text{m}}L^3}\left(1+\varepsilon_{\text{pre}}\right)^3+8}{30\pi\frac{E_{\text{r}}h_{\text{r}}}{E_{\text{m}}L}\varepsilon_{\text{pre}}\left(1+\varepsilon_{\text{pre}}\right)^2+5\pi^3\frac{E_{\text{r}}h_{\text{r}}^3}{E_{\text{m}}L^3}\left(1+\varepsilon_{\text{pre}}\right)^3+8}. \tag{13}$$

It should be pointed out that η approaches to 1, therefore α in Eq. (12) remains finite, at the limit $\varepsilon_{\text{pre}}\to 0$.

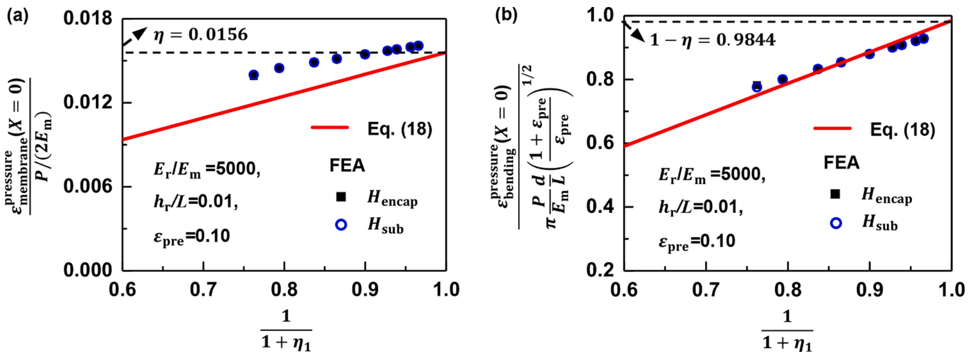

Fig. 5. The membrane strain $\varepsilon^{pressure}_{membrane}$ (a) and bending strain $\varepsilon^{pressure}_{bending}$ (b) in Si-NM located at $X = 0$ (midpoint between two bonding sites) versus $\frac{1}{1+\eta_1}$, to validate the analytic model for finite-thickness encapsulation/substrate under pressure. The Si-NM is located at the bottom of the ribbon with $d = 0.5h_r$. The symbols denote FEA results for a range of encapsulation/substrate thickness, and the lines denote analytic results.

The strain in Si-NM (piezoresistive strain gauge) depends on its location (specifically, the distance d from the neutral mechanical plane of the ribbon) and is given by

$$\varepsilon^{pressure}_{sensor} = \varepsilon^{pressure}_{membrane} + \varepsilon^{pressure}_{bending}, \tag{14}$$

and the membrane and bending strains are

$$\varepsilon^{pressure}_{membrane} = \frac{P}{2E_m}\eta,\ \varepsilon^{pressure}_{bending} = \pi\frac{P}{E_m}\frac{d}{L}\left(\frac{1+\varepsilon_{pre}}{\varepsilon_{pre}}\right)^{1/2}(1-\eta)\cos\left(\frac{2\pi X}{L}\right), \tag{15}$$

where d is the distance of the Si-NM to the neutral mechanical plane (Fig. 2a, $d = \frac{1}{2}h_r$ when the Si-NM is on the bottom of the ribbon). The bending strain in the above equation vanishes at the limit $\varepsilon_{pre} \to 0$. As shown in Fig. 4, the membrane and bending strains in the above equation are validated by FEA without any parameter fitting, for the Si-NM location $X = 0$ (crest of the wavy ribbon) and $d = \frac{1}{2}h_r$ (the bottom of the ribbon), and a wide range of material and geometry parameters and pre-strain with the baseline values $E_r = 2.5$ GPa, $E_m = 500$ kPa, $h_r = 5$ μm, $L = 500$ μm and $\varepsilon_{pre} = 0.10$ that are representative in experiments (Sun et al., 2006; Xu et al., 2015; Zhang et al., 2015b; Won et al., 2019).

2.3. Encapsulation and substrate with finite thickness

The encapsulation and substrate with the finite thickness H_{encap} and H_{sub} are studied in this section. For simplicity they are still assumed to have the same elastic properties. The analysis in Section 2.2, specifically Eqs. (4)-(10), still hold, but the remote boundary conditions of applied pressure P and zero shear are imposed at $z = H_{encap}$ and $z = -H_{sub}$. The parameters α and β in Eqs. (4) and (5) become (see Appendix C for details)

$$\alpha = -\frac{1-\eta}{4\varepsilon_{pre}(1+\varepsilon_{pre})(1+\eta_1)},\ \beta = \frac{1}{2(1+\eta_1)}, \tag{16}$$

which are simply Eq. (12) for the semi-infinite encapsulation and substrate multiplied by $\frac{1}{1+\eta_1}$ to account for the effect of finite thickness, where η_1 is given by

$$\eta_1 = \frac{E_r h_r}{E_m(H_{encap}+H_{sub})}\eta, \tag{17}$$

and η in the above equation and Eq. (16) is still given in Eq. (13).

The strain in Si-NM is still given by Eq. (14), and the membrane and bending strains are the same as Eq. (15), except by a factor $\frac{1}{1+\eta_1}$ to account for the effect of finite thickness. i.e.,

$$\varepsilon^{pressure}_{membrane} = \frac{P}{2E_m}\frac{\eta}{1+\eta_1},\ \varepsilon^{pressure}_{bending} = \pi\frac{P}{E_m}\frac{d}{L}\left(\frac{1+\varepsilon_{pre}}{\varepsilon_{pre}}\right)^{1/2}\frac{1-\eta}{1+\eta_1}\cos\left(\frac{2\pi X}{L}\right). \tag{18}$$

As shown in Fig. 5, the membrane and bending strains in the above equation are validated by FEA without any parameter fitting, for the Si-NM location $X = 0$ (the crest of the wavy ribbon) and $d = \frac{1}{2}h_r$ (the bottom of the ribbon), and a range of encapsulation and substrate thickness, with the baseline values $H_{encap} = 1$ mm and $H_{sub} = 1$ mm. The baseline values for the other material and geometry properties and pre-strain are the same as those in Section 2.2. Some deviation is observed in the membrane strain (Fig. 5a) since the membrane strain is assumed to be strictly uniform in the theoretical model. This deviation does not affect the total strain (membrane

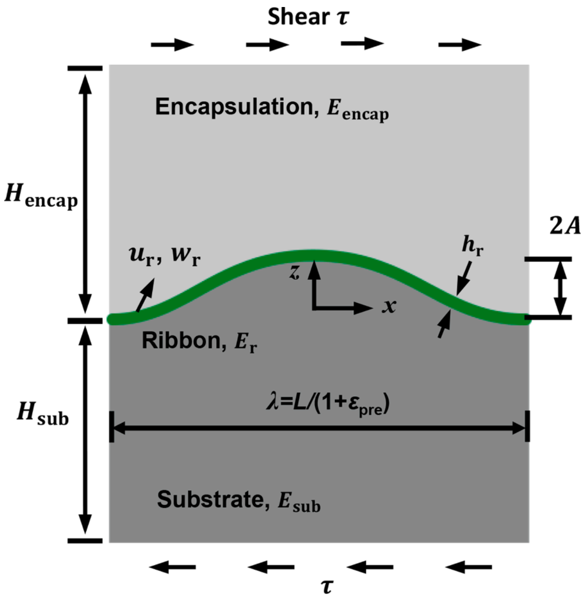

Fig. 6. Schematic of the model of a single unit cell under shear stress.

strain + bending strain) in Si-NM greatly, as for typical parameters around the baseline values, the membrane strain is usually much smaller than the bending strain.

2.4. Encapsulation and substrate of different materials

For the encapsulation and substrate with the different elastic moduli $E_{encap}$and E_{sub} (Kim et al., 2009; Li et al., 2019; Won et al., 2019), the analysis in Section 2.2 is modified to reflect the effect of different elastic moduli (see Appendix C for details). For simplicity, the elastomer that fills the gap between the ribbon and the substrate is assumed to have the same elastic properties as the substrate, and the error due to this assumption is a few percent (See Fig. B2a in Appendix B). The strain in Si-NM is still given by Eq. (14), and the membrane and bending strains now become

$$\varepsilon_{\text{membrane}}^{\text{pressure}} = \frac{P}{2\frac{E_{\text{encap}}H_{\text{encap}}+E_{\text{sub}}H_{\text{sub}}}{H_{\text{encap}}+H_{\text{sub}}}} \frac{\eta}{1+\eta_1}, \tag{19}$$

$$\varepsilon_{\text{bending}}^{\text{pressure}} = \pi \frac{P}{\frac{E_{\text{encap}}H_{\text{encap}}+E_{\text{sub}}H_{\text{sub}}}{H_{\text{encap}}+H_{\text{sub}}}} \frac{d}{L}\left(\frac{1+\varepsilon_{\text{pre}}}{\varepsilon_{\text{pre}}}\right)^{1/2} \frac{1-\eta}{1+\eta_1}\cos\left(\frac{2\pi X}{L}\right), \tag{20}$$

where η and η_1 are given by

$$\eta = \frac{5\pi^3 \frac{E_r h_r^3}{\frac{E_{\text{encap}}+E_{\text{sub}}}{2}L^3}\left(1+\varepsilon_{\text{pre}}\right)^3 + 8}{30\pi \frac{E_r h_r}{\frac{E_{\text{encap}}+E_{\text{sub}}}{2}L}\varepsilon_{\text{pre}}\left(1+\varepsilon_{\text{pre}}\right)^2 + 5\pi^3 \frac{E_r h_r^3}{\frac{E_{\text{encap}}+E_{\text{sub}}}{2}L^3}\left(1+\varepsilon_{\text{pre}}\right)^3 + 8}, \tag{21}$$

$$\eta_1 = \frac{E_r h_r}{E_{\text{encap}}H_{\text{encap}} + E_{\text{sub}}H_{\text{sub}}}\eta - \frac{\left(E_{\text{encap}} - E_{\text{sub}}\right)A}{E_{\text{encap}}H_{\text{encap}} + E_{\text{sub}}H_{\text{sub}}}, \tag{22}$$

where $A = \frac{L}{\pi}\sqrt{\frac{\varepsilon_{\text{pre}}}{1+\varepsilon_{\text{pre}}} - \varepsilon_c} \approx \frac{L}{\pi}\sqrt{\frac{\varepsilon_{\text{pre}}}{1+\varepsilon_{\text{pre}}}}$ is the amplitude after pre-strain release (before the pressure is applied). The above two equations degenerate to Eqs. (13) and (17) for the encapsulation and substrate of the same material.

3. Shear stress sensing

The analytic model is developed for the encapsulated wavy ribbon under remote shear. The processes to form the encapsulated wavy ribbon are the same as those in Section 2.1, and the representative unit cell is the same as that in Section 2.4, except that the pressure is replaced by the remote shear stress τ, as shown in Fig. 6.

For the applied shear stress much smaller than the elastic modulus of the encapsulation and substrate, $\tau << E_{encap}, E_{sub}$, the induced displacement is small and linearly elastic. FEA (see Appendix B) suggests that the out-of-plane displacement of the wavy ribbon under

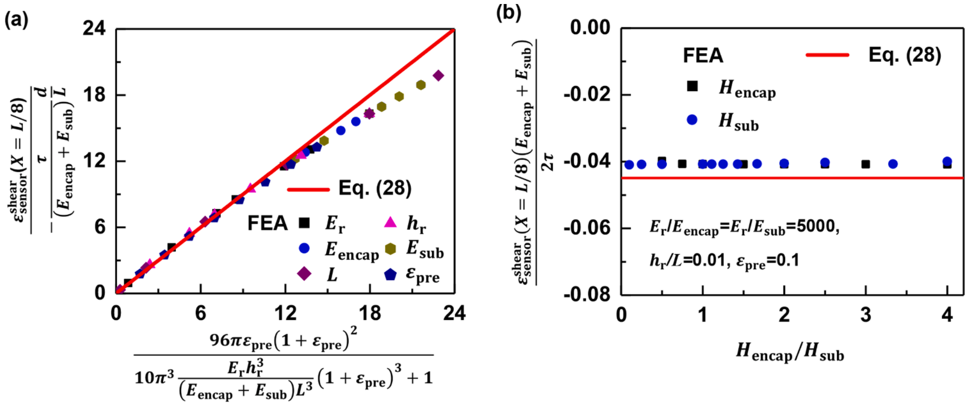

Fig. 7. (a) Validation of the analytic solution for shear given in Eq. (28). The Si-NM is located at $X = L/8$ and at the bottom of the ribbon with $d = 0.5h_r$. (b) The strain in Si-NM versus the encapsulation and substrate thickness. The symbols denote FEA results for a range of material and geometric parameters as well as the pre-strain, and the lines denote analytic results.

shear stress is well approximated by

$$w_r = \frac{2\tau}{E_{encap} + E_{sub}} \omega A \sin\left(\frac{4\pi x}{\lambda}\right), \tag{23}$$

where the dimensionless parameter ω is to be determined and is independent of τ. For the same reason discussed in Section 2.2, the membrane strain is almost uniform in the ribbon, which is confirmed by FEA (See Figs. B1c and B1d in Appendix B). The uniformity of the membrane strain in the ribbon $\varepsilon_{11} = \frac{d(u_0+u_r)}{dx} + \frac{1}{2}\left[\frac{d(w_0+w_r)}{dx}\right]^2$ gives the in-plane displacement u_r as

$$u_r = \frac{2\tau}{E_{encap} + E_{sub}}\left[2\pi\omega\frac{A^2}{\lambda}\cos\left(\frac{2\pi x}{\lambda}\right) - \frac{2\pi}{3}\omega\frac{A^2}{\lambda}\cos\left(\frac{6\pi x}{\lambda}\right) + \psi x\right], \tag{24}$$

where the dimensionless parameter ψ is to be determined, and only terms that are linear with τ are kept. The membrane energy and the bending energy in the ribbon per period are (See Appendix E for details)

$$U_{membrane}^{shear} = \frac{2\tau^2}{(E_{encap} + E_{sub})^2} E_r h_r \lambda \psi^2, \quad U_{bending}^{shear} = \frac{\tau^2}{(E_{encap} + E_{sub})^2} E_r h_r^3 \frac{64\pi^4 A^2}{3\lambda^3}\omega^2, \tag{25}$$

respectively.

The displacements u and w in the encapsulation and substrate satisfy the equations of force equilibrium given in Eqs. (8) and (9). The continuity conditions of displacements across the encapsulation/ribbon and ribbon/substrate interfaces are the same as Eq. (10) with u_r and w_r given in Eqs. (23) and (24). The remote boundary conditions are the applied shear stress τ and zero normal stress at the top of the encapsulation ($z = H_{encap}$) and the bottom of the substrate ($z = -H_{sub}$). The solutions to the displacements of the encapsulation and substrate are given in Appendix F, which lead to the strain energy U_{encap}^{shear} and U_{sub}^{shear} (quadratic functions of ω and ψ) in the encapsulation and substrate, and the external work W_{encap}^{shear} and W_{sub}^{shear} (linear functions of ω and ψ) due to the applied shear stress τ on the top of the encapsulation and on the bottom of the substrate, respectively (See Appendix E for details). The total potential energy is

$$\Pi^{shear}(\omega, \psi) = U_{membrane}^{shear} + U_{bending}^{shear} + U_{encap}^{shear} + U_{sub}^{shear} - W_{encap}^{shear} - W_{sub}^{shear}, \tag{26}$$

where the first two terms are given in Eq. (25). Minimizing the total potential energy via $\frac{\partial \Pi^{shear}}{\partial \omega} = \frac{\partial \Pi^{shear}}{\partial \psi} = 0$ gives the two variables ω and ψ as (see Appendix F for details)

$$\omega = \frac{3\left[\varepsilon_{pre}(1+\varepsilon_{pre})\right]^{1/2}}{10\pi^3 \frac{E_r h_r^3}{(E_{encap}+E_{sub})L^3}(1+\varepsilon_{pre})^3 + 1}, \quad \psi = 0. \tag{27}$$

Here $\psi = 0$ gives zero membrane strain $\varepsilon_{membrane}^{shear}$ (see Appendix E) such that the strain in Si-NM results only from the bending deformation, and is given by

$$\varepsilon_{\text{sensor}}^{\text{shear}} = \varepsilon_{\text{bending}}^{\text{shear}} = -\frac{\tau}{E_{\text{encap}} + E_{\text{sub}}} \frac{d}{L} \frac{96\pi\varepsilon_{\text{pre}}\left(1+\varepsilon_{\text{pre}}\right)^2}{10\pi^3 \frac{E_r h_r^3}{\left(E_{\text{encap}}+E_{\text{sub}}\right)L^3}\left(1+\varepsilon_{\text{pre}}\right)^3 + 1} \sin\left(\frac{4\pi X}{L}\right). \tag{28}$$

As shown in Fig. 7a, the strain in Si-NM is validated by FEA without any parameter fitting, for the Si-NM location $X = L/8$ and $d = \frac{1}{2}h_r$ (the bottom of the ribbon), and a wide range of material and geometry parameters and pre-strain. The baseline values of geometry and material parameters and pre-strain are the same as those in Section 2. The strain in Si-NM is independent of the encapsulation/substrate thickness, which is validated by FEA (Fig. 7b).

4. Concluding remarks and discussions

This paper presents analytic solutions for encapsulated, buckled ribbons under remotely applied pressure and shear stress. The solution, which accounts for the wavy (buckled) structure and is validated by FEA, is obtained in terms of the ribbon, encapsulation and substrate material and geometric properties, as well as the pre-strain applied to the substrate. The results are useful for the simultaneous measurement of the pressure and shear stress via two Si-NMs placed on a flat ribbon before its buckling, which is important to the development of tactile sensors.

For simultaneously applied pressure P and remote shear stress τ, the strain in the Si-NM is the linear superposition[1] of those in Eqs. (14) and (28). This suggests the determination of P and τ via two Si-NMs (sensors). The first Si-NM (sensor 1) is placed at $X = 0$ (midpoint between two bonding sites), which is most sensitive (with respect to X) to pressure P, and is independent to the shear stress τ (See Figs. B1b and B1d) such that P can be determined from sensor 1. The second Si-NM (sensor 2) is placed at $X = L/8$ (or $X = -L/8$, $\pm 3L/8$) (1/8 of the spacing between bonding sides, measured from the midpoint or a bonding site), which is most sensitive to the shear stress τ (See Fig. B1d) such that τ can be determined (after P is determined from sensor 1).

In a more general case, the shear stress has two in-plane components (τ_x along X- direction and τ_y along Y- direction, see Fig. G1), which can be measured, together with the normal pressure P, by the sensor based on an array of table-like 3D structures (Won et al., 2019). The analytic solutions presented in this work, although are developed for 2D wavy ribbon structure, can be extended to scaling laws to account for the complexity of 3D structure.

In practical applications, the pressure/shear stress may be non-uniform. Based on the analytic model proposed in this manuscript, a design to determine the non-uniform pressure/shear stress is presented in Fig. G2. The device consists of several units (pixels). The deformation of these units is not coupled such that each unit can determine the average pressure/shear stress applied on top of the encapsulation, without the interfering from other units. Each unit consists of a few periods of the wavy ribbon and the strain gauges are integrated in the middle period, such that the periodic boundary conditions adopted by the analytic model in Section 2 and 3 apply and the analytical solutions may provide design guidelines to this design.

The design/analytic solution/FEA presented in the manuscript may also be extended to account for the effect of the soft and curved surface (e.g. skin, see Fig. G3) below the sensor, which is common in applications. Further discussions with theoretical models (e.g. scaling laws) and FEA will be published in a future paper.

Declaration of Competing Interest

The authors declare no conflicts of interests

Acknowledgments

X.Y. thanks the support from the China Scholarship Council (No. 201806120080). Y. W. acknowledges the support from the National Natural Science Foundation of China (No. 51790502). S.M.W. acknowledges supports by the National Research Foundation of Korea (NRF) grant funded by the Korea government (MSIP; Ministry of Science, ICT & Future Planning; grant No. 2020R1G1A1101267), and by Nano Material Technology Development Program (2020M3H4A1A03084600) funded by the Ministry of Science and ICT of Korea.

Appendix A. $u_0(x)$ and $w_0(x)$ in the deformed configuration

Substitution of the coordinate X in the undeformed configuration by $X = x - u_0$ into u_0 in Eq. (1) yields

$$u_0 = \frac{\pi A^2}{4L}\sin\left[\frac{4\pi(x-u_0)}{L}\right] - \frac{\varepsilon_{\text{pre}}}{1+\varepsilon_{\text{pre}}}(x-u_0). \tag{A.1}$$

Its Taylor Series expansion with respect to u_0 leads to the solution in Eq. (3), after the terms $O\left(\frac{A^2}{L^2}\right)$ are neglected (with respect to 1). Similarly, substitution of $X = x - u_0$ into w_0 in Eq. (1) yields the solution in Eq. (2).

[1] FEA suggests that the strain in Si-NM is nearly linear with the pressure for $P \le 0.1\frac{E_{\text{encap}}H_{\text{encap}}+E_{\text{sub}}H_{\text{sub}}}{H_{\text{encap}}+H_{\text{sub}}}$ and with the shear stress for $\tau \le 0.025(E_{\text{encap}} + E_{\text{sub}})$ (see Fig. B3). Beyond the ranges, the linear superposition no longer holds.

Appendix B. Finite element analysis

The FEA software ABAQUS is used to determine the deformation of the encapsulated wavy ribbon. Periodic boundary conditions are applied on the two sides of the unit cell at $x = \pm\lambda/2$, as shown in Figs. 3 and 6. The linear-elastic elastomeric encapsulation and substrate are modeled by the four-node plane-stress elements (CPS4), whereas the linear-elastic wavy ribbon is modeled by the two-node linear beam elements (B21) with all degrees of translational freedom constrained to those of the plane-stress elements at the encapsulation/ribbon and ribbon/substrate interfaces.

For remotely applied pressure, Fig. B1a shows that the shear tractions at the encapsulation/ribbon and ribbon/substrate interfaces are almost equal and opposite such that the net shear force on the ribbon is nearly zero. This leads to the nearly uniform membrane strain in the ribbon due to force equilibrium, as shown in Fig. B1b. The same conclusions also hold for the remotely applied shear, as shown in Figs. B1c and B1d.

Fig. B2 a justifies the assumption in Sections 2.4 and 3 that the elastomer filling the gap between the ribbon and the substrate has the same elastic properties as the substrate. It shows the sensor strain under remote pressure obtained by FEA without this assumption,

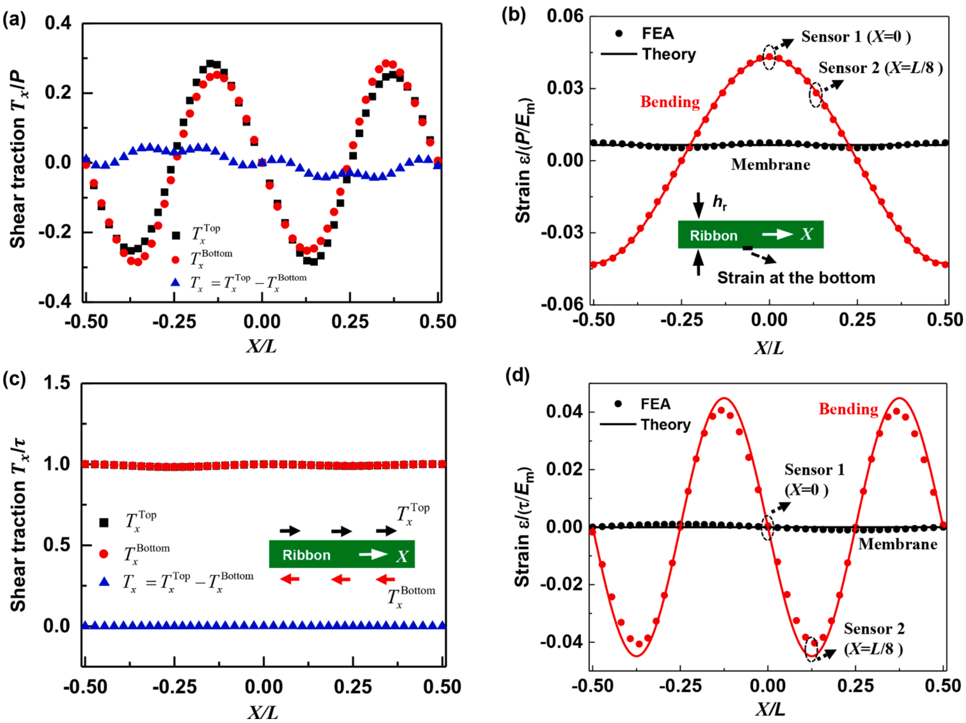

Fig. B1. Justification for the assumption of uniform membrane strain in the ribbon: (a, b) pressure; (c,d) shear. The shear tractions applied on the top (solid squares) and bottom (solid circles) of the ribbon are approximately equal and are opposite for both (a) pressure and (c) shear. The membrane strains in the ribbon are uniform and are much smaller than the bending strains for both (b) pressure and (d) shear. Here baseline values for the material and geometry properties and pre-strain are used.

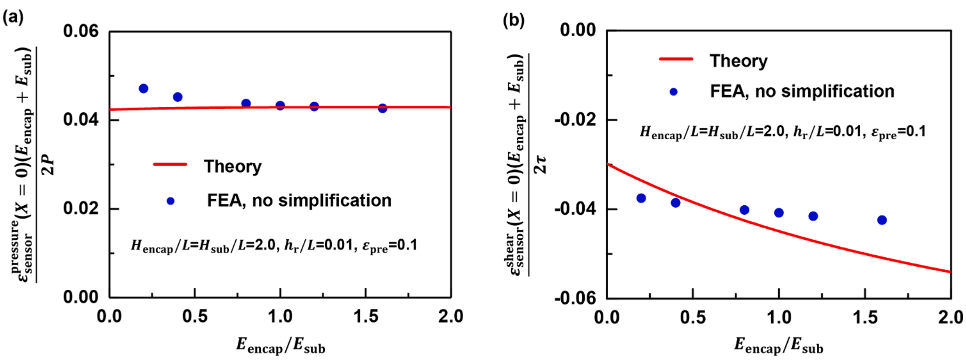

Fig. B2. Justification for the assumption that the elastomer between the ribbon and substrate is the same material as substrate: (a) pressure; (b) shear. Here baseline values for the material and geometry properties and pre-strain are used.

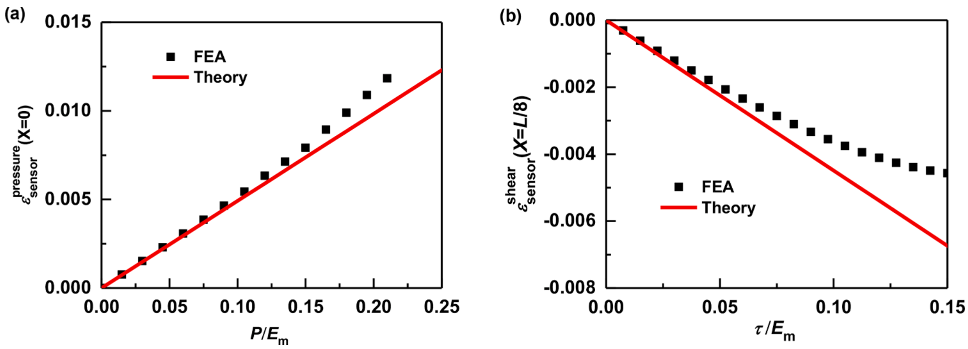

Fig. B3. The strain in Si-NM versus the applied (a) pressure P and (b) shear stress τ. Here baseline values for the material and geometry properties and pre-strain are used.

which agrees reasonably well with the analytic model (under this assumption) for various $E_{\rm encap}/E_{\rm sub}$. Similar conclusions hold for the remotely applied shear, as shown in Fig. B2b.

Fig. B3 shows that the relationship of the strain in Si-NM versus normal pressure P and shear stress τ is in the linear range when $P \le 0.1E_{\rm m}$ and $\tau \le 0.05E_{\rm m}$. For baseline values ($E_{\rm m} = 500$ kPa), the linear ranges for pressure P and shear stress τ are 0~50 kPa and 0~25 kPa, respectively, which are larger than those of previous flexible pressure/shear sensors (0~10 kPa in Boutry et al., 2018) and sufficient for practical use.

Appendix C. The total potential energy of the unit cell under pressure

For the encapsulation (modulus $E_{\rm encap}$, Poisson's ratio $\upsilon_{\rm encap} = 0.5$, thickness $H_{\rm encap}$) and substrate (modulus $E_{\rm sub}$, Poisson's ratio $\upsilon_{\rm sub} = 0.5$, thickness $H_{\rm sub}$) of different materials and finite thickness, the ribbon displacements have the same forms as Eqs. (4) and (5) with $E_{\rm m}$ replaced by $\frac{E_{\rm encap}H_{\rm encap}+E_{\rm sub}H_{\rm sub}}{H_{\rm encap}+H_{\rm sub}}$, i.e.

$$u_{\rm r} = \frac{P\left(H_{\rm encap}+H_{\rm sub}\right)}{E_{\rm encap}H_{\rm encap}+E_{\rm sub}H_{\rm sub}}\left[\frac{\pi}{2}\alpha\frac{A^2}{\lambda}\sin\left(\frac{4\pi x}{\lambda}\right)+\beta x\right], \tag{C.1}$$

$$w_{\rm r} = \frac{P\left(H_{\rm encap}+H_{\rm sub}\right)}{E_{\rm encap}H_{\rm encap}+E_{\rm sub}H_{\rm sub}}\alpha A\cos\left(\frac{2\pi x}{\lambda}\right). \tag{C.2}$$

The membrane energy of the wavy ribbon per period is obtained by

$$\begin{aligned} U_{\rm membrane}^{\rm pressure} &= \int_{-\lambda/2}^{\lambda/2}\frac{1}{2}E_{\rm r}h_{\rm r}\left(\frac{{\rm d}u_{\rm r}}{{\rm d}x}+\frac{{\rm d}w_0}{{\rm d}x}\frac{{\rm d}w_{\rm r}}{{\rm d}x}\right)^2\sqrt{1+\left(\frac{{\rm d}w_0}{{\rm d}x}\right)^2}{\rm d}x \\ &\approx \frac{P^2\left(H_{\rm encap}+H_{\rm sub}\right)^2}{\left(E_{\rm encap}H_{\rm encap}+E_{\rm sub}H_{\rm sub}\right)^2}E_{\rm r}h_{\rm r}\lambda\left(\frac{2\pi^4A^4}{\lambda^4}\alpha^2+\frac{2\pi^2A^2}{\lambda^2}\alpha\beta+\frac{1}{2}\beta^2\right), \end{aligned} \tag{C.3}$$

where the curve length $\sqrt{1+\left(\frac{{\rm d}w_0}{{\rm d}x}\right)^2}{\rm d}x = \left[1+O\left(\frac{A^2}{\lambda^2}\right)\right]{\rm d}x \approx {\rm d}x$. Similarly, the bending energy of the wavy ribbon is obtained by

$$U_{\rm bending}^{\rm pressure} = \int_{-\lambda/2}^{\lambda/2}\frac{1}{24}E_{\rm r}h_{\rm r}^3\left(\frac{{\rm d}^2w_{\rm r}}{{\rm d}x^2}\right)^2\sqrt{1+\left(\frac{{\rm d}w_0}{{\rm d}x}\right)^2}{\rm d}x \approx \frac{P^2\left(H_{\rm encap}+H_{\rm sub}\right)^2}{\left(E_{\rm encap}H_{\rm encap}+E_{\rm sub}H_{\rm sub}\right)^2}E_{\rm r}h_{\rm r}^3\frac{\pi^4A^2}{3\lambda^3}\alpha^2. \tag{C.4}$$

The membrane strain and bending strain in Eq. (C.3) and Eq. (C.4) are derived from the von Karman elastic plate theory (Landau and Lifshitz, 1959) by neglecting high-order terms. For the encapsulation and substrate of finite thicknesses, their displacements induced by the pressure are presented in Appendix D. The strain energies in the encapsulation and substrate are then given by

$$\begin{aligned} U_{\rm encap}^{\rm pressure} &= \frac{P^2\left(H_{\rm encap}+H_{\rm sub}\right)^2}{\left(E_{\rm encap}H_{\rm encap}+E_{\rm sub}H_{\rm sub}\right)^2}E_{\rm encap}\lambda^2\left(\frac{4\pi A^2}{15\lambda^2}\alpha^2+\frac{H_{\rm encap}-A}{2\lambda}\beta^2\right) \\ &+\frac{\pi}{10}\frac{P^2\left(H_{\rm encap}+H_{\rm sub}\right)}{\left(E_{\rm encap}H_{\rm encap}+E_{\rm sub}H_{\rm sub}\right)}\lambda A(2\alpha+\beta)+\frac{3}{8}\frac{P^2}{E_{\rm encap}}\lambda\left(H_{\rm encap}-A\right), \end{aligned} \tag{C.5}$$

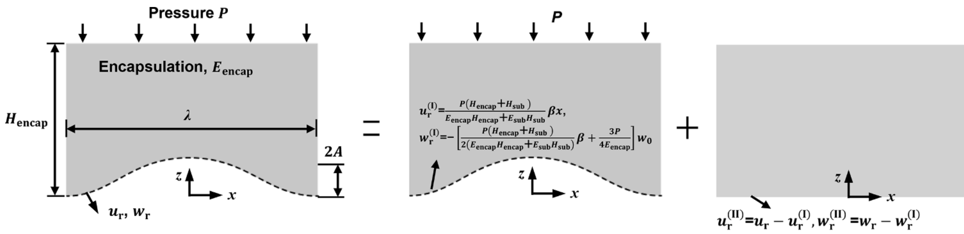

Fig. D1. Decomposition of the deformation of the encapsulation under remote pressure into two parts.

$$
\begin{aligned}
U_{\mathrm{sub}}^{\mathrm{pressure}} = & \frac{P^2\left(H_{\mathrm{encap}}+H_{\mathrm{sub}}\right)^2}{\left(E_{\mathrm{encap}}H_{\mathrm{encap}}+E_{\mathrm{sub}}H_{\mathrm{sub}}\right)^2}E_{\mathrm{sub}}\lambda^2\left(\frac{4\pi A^2}{15\lambda^2}\alpha^2+\frac{H_{\mathrm{sub}}+A}{2\lambda}\beta^2\right) \\
& -\frac{\pi}{10}\frac{P^2\left(H_{\mathrm{encap}}+H_{\mathrm{sub}}\right)}{\left(E_{\mathrm{encap}}H_{\mathrm{encap}}+E_{\mathrm{sub}}H_{\mathrm{sub}}\right)}\lambda A(2\alpha+\beta)+\frac{3}{8}\frac{P^2}{E_{\mathrm{sub}}}\lambda(H_{\mathrm{sub}}+A),
\end{aligned}
\tag{C.6}
$$

where the terms that induce errors $O\left(\frac{A^2}{\lambda^2}\right)$ to α and β (as compared to 1) are neglected.

The external works due to the pressure on the top of the encapsulation and the bottom of the substrate are obtained by

$$
W_{\mathrm{encap}}^{\mathrm{pressure}} = \int_{-\lambda/2}^{\lambda/2}(-P)\cdot w\left(z=H_{\mathrm{encap}}\right)\mathrm{d}x = \frac{P^2\left(H_{\mathrm{encap}}+H_{\mathrm{sub}}\right)}{2\left(E_{\mathrm{encap}}H_{\mathrm{encap}}+E_{\mathrm{sub}}H_{\mathrm{sub}}\right)}\lambda\left(H_{\mathrm{encap}}-A\right)\beta+\frac{3P^2}{4E_{\mathrm{encap}}}\lambda\left(H_{\mathrm{encap}}-A\right),
\tag{C.7}
$$

$$
W_{\mathrm{sub}}^{\mathrm{pressure}} = \int_{-\lambda/2}^{\lambda/2}P\cdot w(z=-H_{\mathrm{sub}})\mathrm{d}x = \frac{P^2\left(H_{\mathrm{encap}}+H_{\mathrm{sub}}\right)}{2\left(E_{\mathrm{encap}}H_{\mathrm{encap}}+E_{\mathrm{sub}}H_{\mathrm{sub}}\right)}\lambda(H_{\mathrm{sub}}+A)\beta+\frac{3P^2}{4E_{\mathrm{sub}}}\lambda(H_{\mathrm{sub}}+A).
\tag{C.8}
$$

The total potential energy of the system Π^{pressure} consist of the above energies and works as shown in Eq. (11). Minimizing the total potential energy Π^{pressure} via $\frac{\partial\Pi^{\mathrm{pressure}}}{\partial\alpha} = \frac{\partial\Pi^{\mathrm{pressure}}}{\partial\beta} = 0$ gives

$$
\alpha = -\frac{1-\eta}{4\varepsilon_{\mathrm{pre}}\left(1+\varepsilon_{\mathrm{pre}}\right)(1+\eta_1)},\ \beta = \frac{1}{2(1+\eta_1)},
\tag{C.9}
$$

where η and η_1 are given in Eqs. (21) and (22), respectively. With $\cos\left(\frac{2\pi x}{\lambda}\right) = \cos\left(\frac{2\pi X}{L}\right)+O\left(\frac{A^2}{L^2}\right)\approx\cos\left(\frac{2\pi X}{L}\right)$, the membrane and bending strains in Si-NM induced by the pressure are obtained from (Landau and Lifshitz, 1959)

$$
\varepsilon_{\mathrm{membrane}}^{\mathrm{pressure}} = \frac{\mathrm{d}u_{\mathrm{r}}}{\mathrm{d}x}+\frac{\mathrm{d}w_0}{\mathrm{d}x}\frac{\mathrm{d}w_{\mathrm{r}}}{\mathrm{d}x},\ \varepsilon_{\mathrm{bending}}^{\mathrm{pressure}} = d\frac{\mathrm{d}^2w_{\mathrm{r}}}{\mathrm{d}x^2},
\tag{C.10}
$$

and are given in Eq. (18).

For the encapsulation and substrate of the same material ($E_{\mathrm{encap}} = E_{\mathrm{sub}} = E_{\mathrm{m}}$), α and βin Eq. (C.9) become the same as Eq. (16) with η and η_1 in Eqs. (21) and (22) degenerating to Eqs. (13) and (17), respectively. Their limits $H_{\mathrm{encap}}\to+\infty$ and $H_{\mathrm{sub}}\to+\infty$ yield α and β in Eq. (12), with η given in Eq. (13), for semi-infinite encapsulation and substrate.

Appendix D. The displacements in the encapsulation and substrate under pressure

This appendix focuses on deformation in the encapsulation under pressure, and that in the substrate can be obtained similarly. The boundary conditions at the top of the encapsulation are

$$
\sigma_z = \frac{E_{\mathrm{encap}}}{1-\upsilon_{\mathrm{encap}}^2}\left(\frac{\partial w}{\partial z}+\upsilon_{\mathrm{encap}}\frac{\partial u}{\partial x}\right) = -P,\ \tau_{xz} = \frac{E_{\mathrm{encap}}}{2\left(1+\upsilon_{\mathrm{encap}}\right)}\left(\frac{\partial u}{\partial z}+\frac{\partial w}{\partial x}\right) = 0 \text{at } z = H_{\mathrm{encap}}.
\tag{D.1}
$$

The continuity of displacements across the encapsulation/ribbon interface requires the displacements at the wavy boundary $z = w_0(x)$ to be the same as those in Eqs. (C.1) and (C.2).

The displacements are decomposed into two parts (See Fig. D1), i.e. $u = u^{(\mathrm{I})}+u^{(\mathrm{II})}$ and $w = w^{(\mathrm{I})}+w^{(\mathrm{II})}$, where the first part

$$
u^{(\mathrm{I})} = \frac{P\left(H_{\mathrm{encap}}+H_{\mathrm{sub}}\right)}{E_{\mathrm{encap}}H_{\mathrm{encap}}+E_{\mathrm{sub}}H_{\mathrm{sub}}}\beta x,\ w^{(\mathrm{I})} = -\left[\frac{P\left(H_{\mathrm{encap}}+H_{\mathrm{sub}}\right)}{2\left(E_{\mathrm{encap}}H_{\mathrm{encap}}+E_{\mathrm{sub}}H_{\mathrm{sub}}\right)}\beta+\frac{3P}{4E_{\mathrm{encap}}}\right]z
\tag{D.2}
$$

corresponds to a uniform stress and strain field that satisfies the equilibrium Eqs. (8) and (9), remote boundary conditions in Eq. (D.1), and the change of horizontal displacement over each period being consistent with Eq. (C.1) for the ribbon, i.e., $u^{(\mathrm{I})}\left(x = \frac{\lambda}{2}\right) - u^{(\mathrm{I})}\left(x = -\right.$

$\left.\frac{\lambda}{2}\right) = \frac{P(H_{encap}+H_{sub})}{E_{encap}H_{encap}+E_{sub}H_{sub}}\beta\lambda$. The second part ($u^{(II)}$ and $w^{(II)}$) satisfies the equilibrium Eqs. (8) and (9) and vanishing remote tractions

$$\sigma_z^{(II)} = 0, \quad \tau_{xz}^{(II)} = 0 \text{at } z = H_{encap}. \tag{D.3}$$

The displacement continuity across the encapsulation/ribbon interface in Eq. (10) gives$u^{(II)}(z = w_0) = \frac{P(H_{encap}+H_{sub})}{E_{encap}H_{encap}+E_{sub}H_{sub}}\frac{\pi A^2}{2\lambda}\alpha\sin\left(\frac{4\pi x}{\lambda}\right)$ and $w^{(II)}(z = w_0) = \frac{P(H_{encap}+H_{sub})}{E_{encap}H_{encap}+E_{sub}H_{sub}}A\alpha\cos\left(\frac{2\pi x}{\lambda}\right) + \left[\frac{P(H_{encap}+H_{sub})}{2(E_{encap}H_{encap}+E_{sub}H_{sub})}\beta + \frac{3P}{4E_{encap}}\right]w_0$. They can be approximately imposed at $z = 0$, instead of $z = w_0(x)$, i.e.

$$u^{(II)} = \frac{P(H_{encap} + H_{sub})}{E_{encap}H_{encap} + E_{sub}H_{sub}}\frac{\pi A^2}{2\lambda}\alpha\sin\left(\frac{4\pi x}{\lambda}\right)\text{at } z = 0, \tag{D.4}$$

$$w^{(II)} = \frac{P(H_{encap} + H_{sub})}{E_{encap}H_{encap} + E_{sub}H_{sub}}A\alpha\cos\left(\frac{2\pi x}{\lambda}\right) + \left[\frac{P(H_{encap} + H_{sub})}{2(E_{encap}H_{encap} + E_{sub}H_{sub})}\beta + \frac{3P}{4E_{encap}}\right]w_0\text{at } z = 0. \tag{D.5}$$

It can be shown that the errors in the membrane and bending strains of the Si-NM due to the above approximation are on the order of $O\left(\frac{A^2}{\lambda^2}\right)$ (as compared to 1), which are negligible, consistent with the analyses in this paper.

The solution of Eqs. (8), (9), (D.3)~(D.5) is

$$u^{(II)} = C_1 z e^{-\frac{2\pi z}{\lambda}}\sin\left(\frac{2\pi x}{\lambda}\right) + (C_2 + C_3 z)e^{-\frac{4\pi z}{\lambda}}\sin\left(\frac{4\pi x}{\lambda}\right), \tag{D.6}$$

$$\begin{aligned} w^{(II)} = {} & C_1\left(z + \frac{5}{6\pi}\lambda\right)e^{-\frac{2\pi z}{\lambda}}\cos\left(\frac{2\pi x}{\lambda}\right) + \left[C_2 + C_3\left(z + \frac{5}{12\pi}\lambda\right)\right]e^{-\frac{4\pi z}{\lambda}}\cos\left(\frac{4\pi x}{\lambda}\right) \\ & + \left[\frac{P(H_{encap} + H_{sub})}{2(E_{encap}H_{encap} + E_{sub}H_{sub})}\beta + \frac{3P}{4E_{encap}}\right]A, \end{aligned} \tag{D.7}$$

where

$$C_1 = \frac{P(H_{encap} + H_{sub})}{E_{encap}H_{encap} + E_{sub}H_{sub}}\frac{3\pi A}{5\lambda}(2\alpha + \beta) + \frac{P}{E_{encap}}\frac{9\pi A}{10\lambda}, \tag{D.8}$$

$$C_2 = \frac{P(H_{encap} + H_{sub})}{E_{encap}H_{encap} + E_{sub}H_{sub}}\frac{\pi A^2}{2\lambda}\alpha, \tag{D.9}$$

$$C_3 = -\frac{P(H_{encap} + H_{sub})}{E_{encap}H_{encap} + E_{sub}H_{sub}}\frac{6\pi^2 A^2}{5\lambda^2}\alpha. \tag{D.10}$$

Here the encapsulation thickness $H_{encap}/\lambda > 0.5$ such that the errors in Eqs. (D.6)~(D.10) are less than 0.05%.

The displacements of the substrate are similarly obtained as $u = u^{(I)} + u^{(II)}$ and $w = w^{(I)} + w^{(II)}$, with

$$u^{(I)} = \frac{P(H_{encap} + H_{sub})}{E_{encap}H_{encap} + E_{sub}H_{sub}}\beta x, \quad w^{(I)} = -\left[\frac{P(H_{encap} + H_{sub})}{2(E_{encap}H_{encap} + E_{sub}H_{sub})}\beta + \frac{3P}{4E_{sub}}\right]z, \tag{D.11}$$

$$u^{(II)} = C_1 z e^{\frac{2\pi z}{\lambda}}\sin\left(\frac{2\pi x}{\lambda}\right) + (C_2 + C_3 z)e^{\frac{4\pi z}{\lambda}}\sin\left(\frac{4\pi x}{\lambda}\right), \tag{D.12}$$

$$\begin{aligned} w^{(II)} = {} & -C_1\left(z - \frac{5}{6\pi}\lambda\right)e^{\frac{2\pi z}{\lambda}}\cos\left(\frac{2\pi x}{\lambda}\right) - \left[C_2 + C_3\left(z - \frac{5}{12\pi}\lambda\right)\right]e^{\frac{4\pi z}{\lambda}}\cos\left(\frac{4\pi x}{\lambda}\right) \\ & + \left[\frac{P(H_{encap} + H_{sub})}{2(E_{encap}H_{encap} + E_{sub}H_{sub})}\beta + \frac{3P}{4E_{sub}}\right]A, \end{aligned} \tag{D.13}$$

where

$$C_1 = \frac{P(H_{encap} + H_{sub})}{E_{encap}H_{encap} + E_{sub}H_{sub}}\frac{3\pi A}{5\lambda}(2\alpha + \beta) + \frac{P}{E_{sub}}\frac{9\pi A}{10\lambda}, \tag{D.14}$$

$$C_2 = \frac{P(H_{encap} + H_{sub})}{E_{encap}H_{encap} + E_{sub}H_{sub}}\frac{\pi A^2}{2\lambda}\alpha, \tag{D.15}$$

$$C_3 = \frac{P\left(H_{\text{encap}} + H_{\text{sub}}\right)}{E_{\text{encap}}H_{\text{encap}} + E_{\text{sub}}H_{\text{sub}}} \frac{6\pi^2 A^2}{5\lambda^2}\alpha. \tag{D.16}$$

Appendix E. The total potential energy of the unit cell under shear stress

For the ribbon displacements in Eqs. (23) and (24), the membrane energy in the wavy ribbon per period is

$$U^{\text{shear}}_{\text{membrane}} = \int_{-\lambda/2}^{\lambda/2} \frac{1}{2}E_{\text{r}}h_{\text{r}}\left(\frac{\mathrm{d}u_{\text{r}}}{\mathrm{d}x} + \frac{\mathrm{d}w_0}{\mathrm{d}x}\frac{\mathrm{d}w_{\text{r}}}{\mathrm{d}x}\right)^2 \sqrt{1+\left(\frac{\mathrm{d}w_0}{\mathrm{d}x}\right)^2}\mathrm{d}x = \frac{2\tau^2}{\left(E_{\text{encap}} + E_{\text{sub}}\right)^2}E_{\text{r}}h_{\text{r}}\lambda\psi^2, \tag{E.1}$$

where $\sqrt{1+\left(\frac{\mathrm{d}w_0}{\mathrm{d}x}\right)^2}\mathrm{d}x = \left[1 + O\left(\frac{A^2}{\lambda^2}\right)\right]\mathrm{d}x \approx \mathrm{d}x$. The bending energy of the wavy ribbon is

$$U^{\text{shear}}_{\text{bending}} = \int_{-\lambda/2}^{\lambda/2} \frac{1}{24}E_{\text{r}}h_{\text{r}}^3\left(\frac{\mathrm{d}^2 w_{\text{r}}}{\mathrm{d}x^2}\right)^2 \sqrt{1+\left(\frac{\mathrm{d}w_0}{\mathrm{d}x}\right)^2}\mathrm{d}x \approx \frac{\tau^2}{\left(E_{\text{encap}} + E_{\text{sub}}\right)^2}E_{\text{r}}h_{\text{r}}^3\frac{64\pi^4 A^2}{3\lambda^3}\omega^2. \tag{E.2}$$

For the encapsulation and substrate of finite thickness, their displacements induced by the shear stress are provided in Appendix F. The strain energies in the encapsulation and substrate are given by

$$U^{\text{shear}}_{\text{encap}} = \frac{\tau^2}{\left(E_{\text{encap}} + E_{\text{sub}}\right)^2}E_{\text{encap}}\lambda^2\left(\frac{32\pi A^2}{15\lambda^2}\omega^2 + 2\frac{H_{\text{encap}} - A}{\lambda}\psi^2\right) - \frac{\tau^2}{E_{\text{encap}} + E_{\text{sub}}}\frac{32\pi^2 A^3}{5\lambda}\omega + \frac{3}{2}\frac{\tau^2}{E_{\text{encap}}}\left(H_{\text{encap}} - A\right)\lambda, \tag{E.3}$$

$$U^{\text{shear}}_{\text{sub}} = \frac{\tau^2}{\left(E_{\text{encap}} + E_{\text{sub}}\right)^2}E_{\text{sub}}\lambda^2\left(\frac{32\pi A^2}{15\lambda^2}\omega^2 + 2\frac{H_{\text{sub}} + A}{\lambda}\psi^2\right) - \frac{\tau^2}{E_{\text{encap}} + E_{\text{sub}}}\frac{32\pi^2 A^3}{5\lambda}\omega + \frac{3}{2}\frac{\tau^2}{E_{\text{sub}}}\left(H_{\text{sub}} + A\right)\lambda, \tag{E.4}$$

where the terms that induce errors $O\left(\frac{A^2}{\lambda^2}\right)$ to ω and ψ (as compared to 1) are neglected. The external works due to the shear stress on the top of the encapsulation and the bottom of the substrate are obtained by

$$W^{\text{shear}}_{\text{encap}} = \int_{-\lambda/2}^{\lambda/2} \tau \cdot u\left(z = H_{\text{encap}}\right)\mathrm{d}x = \frac{3\tau^2}{E_{\text{encap}}}\lambda\left(H_{\text{encap}} - A\right), \tag{E.5}$$

$$W^{\text{shear}}_{\text{sub}} = \int_{-\lambda/2}^{\lambda/2} (-\tau) \cdot u(z = -H_{\text{sub}})\mathrm{d}x = \frac{3\tau^2}{E_{\text{sub}}}\lambda(H_{\text{sub}} + A). \tag{E.6}$$

The total potential energy per period Π^{shear} consists of the above energies and works as shown in Eq. (26). Minimizing the total potential energy Π^{shear} via $\frac{\partial \Pi^{\text{shear}}}{\partial \omega} = \frac{\partial \Pi^{\text{shear}}}{\partial \psi} = 0$ determines ω and ψ in Eq. (27). With $\sin\left(\frac{4\pi x}{\lambda}\right) = \sin\left(\frac{4\pi X}{L}\right) + O\left(\frac{A^2}{L^2}\right) \approx \sin\left(\frac{4\pi X}{L}\right)$, the membrane strain and the bending strain in the ribbon induced by the shear stress are

$$\varepsilon^{\text{shear}}_{\text{membrane}} = \frac{\mathrm{d}u_{\text{r}}}{\mathrm{d}x} + \frac{\mathrm{d}w_0}{\mathrm{d}x}\frac{\mathrm{d}w_{\text{r}}}{\mathrm{d}x} = 0, \tag{E.7}$$

$$\varepsilon^{\text{shear}}_{\text{bending}} = d\frac{\mathrm{d}^2 w_{\text{r}}}{\mathrm{d}x^2} = -\frac{\tau}{E_{\text{encap}} + E_{\text{sub}}}\frac{d}{L}\frac{96\pi\varepsilon_{\text{pre}}\left(1+\varepsilon_{\text{pre}}\right)^2}{10\pi^3\frac{E_{\text{r}}h_{\text{r}}^3}{\left(E_{\text{encap}} + E_{\text{sub}}\right)L^3}\left(1+\varepsilon_{\text{pre}}\right)^3 + 1}\sin\left(\frac{4\pi X}{L}\right), \tag{E.8}$$

respectively.

Appendix F. The displacements in the encapsulation and substrate under remote shear

This appendix focuses on the deformation in the encapsulation under shear, and that in the substrate can be obtained similarly. At the top of the encapsulation, the stress boundary conditions are

$$\sigma_z = 0, \quad \tau_{xz} = \tau \text{at } z = H_{\text{encap}}. \tag{F.1}$$

The displacements at the encapsulation/ribbon interface $z = w_0(x)$ are given in Eq. (10) with u_{r} and w_{r} in Eqs. (23) and (24). The displacements are decomposed into two parts (See Fig. F1), i.e. $u = u^{(\text{I})} + u^{(\text{II})}$ and $w = w^{(\text{I})} + w^{(\text{II})}$, where the first part

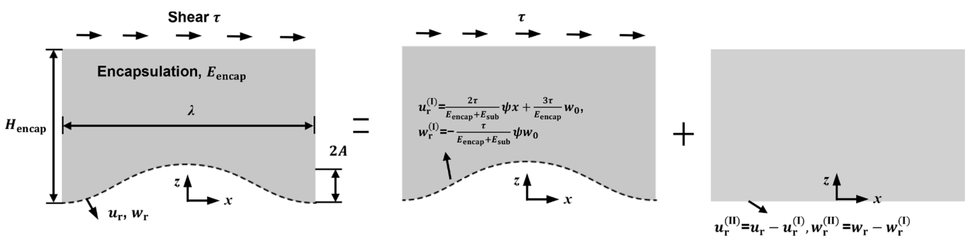

Fig. F1. Decomposition of the deformation of the encapsulation under remote shear stress into two parts.

$$u^{(\text{I})} = \frac{2\tau}{E_{\text{encap}} + E_{\text{sub}}}\psi x + \frac{3\tau}{E_{\text{encap}}}z, \quad w^{(\text{I})} = -\frac{\tau}{E_{\text{encap}} + E_{\text{sub}}}\psi z \tag{F.2}$$

corresponds to a uniform stress and strain field that satisfies the equilibrium Eqs. (8) and (9), remote boundary conditions in Eq. (F.1), and the change of horizontal displacement over each period being consistent with Eq. (24) for the ribbon, i.e., $u^{(\text{I})}\left(x = \frac{\lambda}{2}\right) - u^{(\text{I})}\left(x = -\frac{\lambda}{2}\right) = \frac{2\tau}{E_{\text{encap}}+E_{\text{sub}}}\psi\lambda$. The second part ($u^{(\text{II})}$ and $w^{(\text{II})}$) satisfies the equilibrium Eqs. (8) and (9), vanishing remote tractions given below, and the displacement continuity across the encapsulation/ribbon interface in Eq. (10) but imposed at $z = 0$, i.e.

$$\sigma_z^{(\text{II})} = 0, \quad \tau_{xz}^{(\text{II})} = 0 \text{at } z = H_{\text{encap}}, \tag{F.3}$$

$$u^{(\text{II})} = \frac{\tau}{E_{\text{encap}} + E_{\text{sub}}}\frac{4\pi A^2}{\lambda}\omega\left[\cos\left(\frac{2\pi x}{\lambda}\right) - \frac{1}{3}\cos\left(\frac{6\pi x}{\lambda}\right)\right] - \frac{3\tau}{E_{\text{encap}}}w_0 \text{at } z = 0, \tag{F.4}$$

$$w^{(\text{II})} = \frac{2\tau}{E_{\text{encap}} + E_{\text{sub}}}A\omega\sin\left(\frac{4\pi x}{\lambda}\right) + \frac{\tau}{E_{\text{encap}} + E_{\text{sub}}}\psi w_0 \text{at } z = 0. \tag{F.5}$$

The solution of Eqs. (8), (9), (F.3)~(F.5) is

$$\begin{aligned} u^{(\text{II})} = {} & (C_1 + C_2 z)e^{-\frac{2\pi z}{\lambda}}\cos\left(\frac{2\pi x}{\lambda}\right) + C_3 z e^{-\frac{4\pi z}{\lambda}}\cos\left(\frac{4\pi x}{\lambda}\right) + (C_5 + C_6 z)e^{-\frac{6\pi z}{\lambda}}\cos\left(\frac{6\pi x}{\lambda}\right) \\ & + C_4 z e^{-\frac{2\pi z}{\lambda}}\sin\left(\frac{2\pi x}{\lambda}\right) - \frac{3\tau}{E_{\text{encap}}}A, \end{aligned} \tag{F.6}$$

$$\begin{aligned} w^{(\text{II})} = {} & -\left[C_1 + C_2\left(z + \frac{5}{6\pi}\lambda\right)\right]e^{-\frac{2\pi z}{\lambda}}\sin\left(\frac{2\pi x}{\lambda}\right) - C_3\left(z + \frac{5}{12\pi}\lambda\right)e^{-\frac{4\pi z}{\lambda}}\sin\left(\frac{4\pi x}{\lambda}\right) \\ & - \left[C_5 + C_6\left(z + \frac{5}{18\pi}\lambda\right)\right]e^{-\frac{6\pi z}{\lambda}}\sin\left(\frac{6\pi x}{\lambda}\right) + C_4\left(z + \frac{5}{6\pi}\lambda\right)e^{-\frac{2\pi z}{\lambda}}\cos\left(\frac{2\pi x}{\lambda}\right) + \frac{\tau}{E_{\text{encap}} + E_{\text{sub}}}\psi A, \end{aligned} \tag{F.7}$$

where

$$C_1 = \frac{\tau}{E_{\text{encap}} + E_{\text{sub}}}\frac{4\pi A^2}{\lambda}\omega - \frac{3\tau}{E_{\text{encap}}}A, \tag{F.8}$$

$$C_2 = -\frac{\tau}{E_{\text{encap}} + E_{\text{sub}}}\frac{24\pi^2 A^2}{5\lambda^2}\omega + \frac{\tau}{E_{\text{encap}}}\frac{18\pi A}{5\lambda}, \tag{F.9}$$

$$C_3 = -\frac{\tau}{E_{\text{encap}} + E_{\text{sub}}}\frac{24\pi A}{5\lambda}\omega, \tag{F.10}$$

$$C_4 = \frac{\tau}{E_{\text{encap}} + E_{\text{sub}}}\frac{6\pi A}{5\lambda}\psi, \tag{F.11}$$

$$C_5 = -\frac{\tau}{E_{\text{encap}} + E_{\text{sub}}}\frac{4\pi A^2}{3\lambda}\omega, \tag{F.12}$$

$$C_6 = \frac{\tau}{E_{\text{encap}} + E_{\text{sub}}}\frac{24\pi^2 A^2}{5\lambda^2}\omega. \tag{F.13}$$

The displacements of the substrate are similarly obtained as $u = u^{(\text{I})} + u^{(\text{II})}$ and $w = w^{(\text{I})} + w^{(\text{II})}$, with

$$u^{(\mathrm{I})}=\frac{2\tau}{E_{\mathrm{encap}}+E_{\mathrm{sub}}}\psi x+\frac{3\tau}{E_{\mathrm{sub}}}z,\quad w^{(\mathrm{I})}=-\frac{\tau}{E_{\mathrm{encap}}+E_{\mathrm{sub}}}\psi z. \tag{F.14}$$

$$\begin{aligned}u^{(\mathrm{II})}=&(C_5+C_6z)e^{\frac{2\pi z}{\lambda}}\cos\left(\frac{2\pi x}{\lambda}\right)+C_4ze^{\frac{4\pi z}{\lambda}}\cos\left(\frac{4\pi x}{\lambda}\right)+(C_2+C_3z)e^{\frac{6\pi z}{\lambda}}\cos\left(\frac{6\pi x}{\lambda}\right)\\&+C_1ze^{\frac{2\pi z}{\lambda}}\sin\left(\frac{2\pi x}{\lambda}\right)-\frac{3\tau}{E_{\mathrm{sub}}}A,\end{aligned} \tag{F.15}$$

$$\begin{aligned}w^{(\mathrm{II})}=&\left[C_5+C_6\left(z-\frac{5}{6\pi}\lambda\right)\right]e^{\frac{2\pi z}{\lambda}}\sin\left(\frac{2\pi x}{\lambda}\right)+C_4\left(z-\frac{5}{12\pi}\lambda\right)e^{\frac{4\pi z}{\lambda}}\sin\left(\frac{4\pi x}{\lambda}\right)+\left[C_2+C_3\left(z-\frac{5}{18\pi}\lambda\right)\right]e^{\frac{6\pi z}{\lambda}}\sin\left(\frac{6\pi x}{\lambda}\right)\\&-C_1\left(z-\frac{5}{6\pi}\lambda\right)e^{\frac{2\pi z}{\lambda}}\cos\left(\frac{2\pi x}{\lambda}\right)+\frac{\tau}{E_{\mathrm{encap}}+E_{\mathrm{sub}}}\psi A,\end{aligned} \tag{F.16}$$

where

$$C_1=\frac{\tau}{E_{\mathrm{encap}}+E_{\mathrm{sub}}}\frac{6\pi A}{5\lambda}\psi, \tag{F.17}$$

$$C_2=-\frac{\tau}{E_{\mathrm{encap}}+E_{\mathrm{sub}}}\frac{4\pi A^2}{3\lambda}\omega, \tag{F.18}$$

$$C_3=-\frac{\tau}{E_{\mathrm{encap}}+E_{\mathrm{sub}}}\frac{24\pi^2A^2}{5\lambda^2}\omega, \tag{F.19}$$

$$C_4=-\frac{\tau}{E_{\mathrm{encap}}+E_{\mathrm{sub}}}\frac{24\pi A}{5\lambda}\omega, \tag{F.20}$$

$$C_5=\frac{\tau}{E_{\mathrm{encap}}+E_{\mathrm{sub}}}\frac{4\pi A^2}{\lambda}\omega-\frac{3\tau}{E_{\mathrm{sub}}}A, \tag{F.21}$$

$$C_6=\frac{\tau}{E_{\mathrm{encap}}+E_{\mathrm{sub}}}\frac{24\pi^2A^2}{5\lambda^2}\omega+\frac{\tau}{E_{\mathrm{sub}}}\frac{18\pi A}{5\lambda}. \tag{F.22}$$

Appendix G. Schematics in the concluding remarks and discussions section

Fig. G1 illustrates a unit cell of the pressure/shear sensor based on a 2D array table-like 3D structures with three integrated Si-NMs. The model is periodic along two in-plane (X- and Y-) directions. Fig. G2 shows the device consisting of several units (pixels) with the bottom attaching to a rigid base. Each unit (pixel) consists of a few periods of the wavy ribbon. Fig. G3 illustrates the pressure/shear sensor placing on the soft and curved skin that is commonly encountered in practical applications.

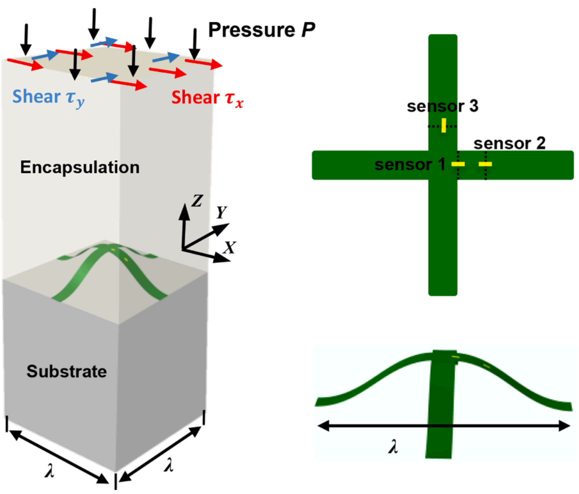

Fig. G1. Schematic of unit cell of the pressure/shear sensor based on a 2D array of table-like 3D structures with three integrated strain gauges.

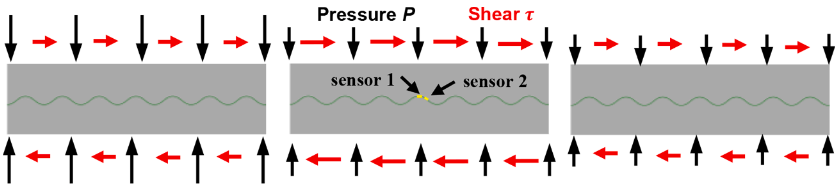

Fig. G2. Schematic of the device consisting of several units (pixels) for determining the non-uniform pressure/shear stress.

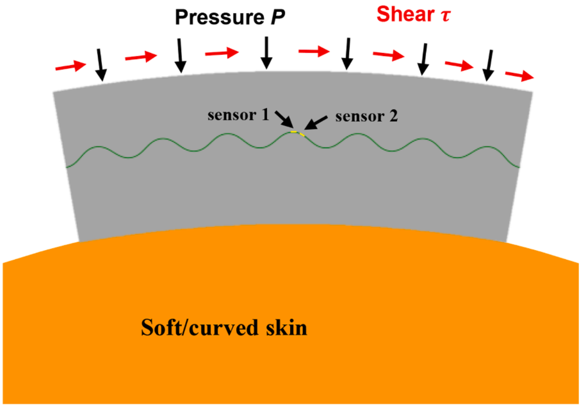

Fig. G3. Schematic of the pressure/shear sensor placed on the soft and curved skin.

References

Al-Mai, O., Ahmadi, M., Albert, J., 2017. A compliant 3-axis fiber-optic force sensor for biomechanical measurement. IEEE Sens. J. 17, 6549–6557.

Bae, G.Y., Han, J.T., Lee, G., Lee, S., Kim, S.W., Park, S., Kwon, J., Jung, S., Cho, K., 2018. Pressure/temperature sensing bimodal electronic skin with stimulus discriminability and linear sensitivity. Adv. Mater. 30, 1803388.

Birznieks, I., Jenmalm, P., Goodwin, A.W., Johansson, R.S., 2001. Encoding of direction of fingertip forces by human tactile afferents. J. Neurosci. 21, 8222–8237.

Boutry, C.M., Negre, M., Jorda, M., Vardoulis, O., Chortos, A., Khatib, O., Bao, Z.N., 2018. A hierarchically patterned, bioinspired e-skin able to detect the direction of applied pressure for robotics. Sci. Robot. 3, eaau6914.

Charalambides, A., Bergbreiter, S., 2017. Rapid manufacturing of mechanoreceptive skins for slip detection in robotic grasping. Adv. Mater. Technol. 2, 1600188.

Chen, H., Zhu, F., Jang, K.I., Feng, X., Rogers, J.A., Zhang, Y.H., Huang, Y., Ma, Y.J., 2018. The equivalent medium of cellular substrate under large stretching, with applications to stretchable electronics. J. Mech. Phys. Solids 120, 199–207.

Chen, H.T., Su, Z.M., Song, Y., Cheng, X.L., Chen, X.X., Meng, B., Song, Z.J., Chen, D.M., Zhang, H.X., 2017. Omnidirectional bending and pressure sensor based on stretchable CNT-PU sponge. Adv. Funct. Mater. 27, 1604434.

Chen, Y.L., Liu, Y.L., Yan, Y., Zhu, Y., Chen, X., 2016. Helical coil buckling mechanism for a stiff nanowire on an elastomeric substrate. J. Mech. Phys. Solids 95, 25–43.

Cheng, M.Y., Lin, C.L., Lai, Y.T., Yang, Y.J., 2010. A polymer-based capacitive sensing array for normal and shear force measurement. Sensors 10, 10211–10225.

Cho, S.H., Lee, S.W., Yu, S., Kim, H., Chang, S., Kang, D., Hwang, I., Kang, H.S., Jeong, B., Kim, E.H., Cho, S.M., Kim, K.L., Lee, H., Shim, W., Park, C., 2017. Micropatterned pyramidal ionic gels for sensing broad-range pressures with high sensitivity. ACS Appl. Mater. Inter. 9, 10128–10135.

Choi, D., Jang, S., Kim, J.S., Kim, H.J., Kim, D.H., Kwon, J.Y., 2019. A highly sensitive tactile sensor using a pyramid-plug structure for detecting pressure, shear force, and torsion. Adv. Mater. Technol. 4, 1800284.

Chortos, A., Liu, J., Bao, Z.N., 2016. Pursuing prosthetic electronic skin. Nat. Mater. 15, 937.

Chu, Z., Sarro, P.M., Middelhoek, S., 1996. Silicon three-axial tactile sensor. Sens. Actuator A-Phys. 54, 505–510.

Chung, H., Kim, B., Lee, J., Lee, J., Xie, Z., Ibler, E., Lee, K., Banks, A., Jeong, J., Kim, J., Ogle, C., Grande, D., Yu, Y., Jang, Assem, P., Ryu, D., Kwak, J., Namkoong, M., Park, J., Lee, Y., Kim, D., Ryu, A., Jeong, J., You, K., Ji, B., Liu, Z., Huo, Q., Feng, X., Deng, Y., Xu, Y., Jang, K., Kim, J., Zhang, Y., Ghaffari, R., Rand, C., Schau, M., Hamvas, A., Weese-Mayer, D., Huang, Y., Lee, S., Lee, C., Shanbhag, N., Paller, A., Xu, S., Rogers, J.A., 2019. Binodal, wireless epidermal electronics systems with in-sensor analytics for neonatal intensive care. Science 363, eaau0780.

Crowder, R., 2006. Toward robots that can sense texture by touch. Science 312, 1478–1479.

Cui, Z., Poblete, F.R., Zhu, Y., 2019. Tailoring the temperature coefficient of resistance of silver nanowire nanocomposites and their application as stretchable temperature sensors. ACS Appl. Mater. Inter. 11, 17836–17842.

Dahiya, R.S., Metta, G., Valle, M., Sandini, G., 2010. Tactile sensing—from humans to humanoids. IEEE T. Robot. 26, 1–20.

Delmas, P., Hao, J., Rodat-Despoix, L., 2011. Molecular mechanisms of mechanotransduction in mammalian sensory neurons. Nat. Rev. Neurosci. 12, 139–153.

Dobrzynska, J.A., Gijs, M.A.M., 2012. Polymer-based flexible capacitive sensor for three-axial force measurements. J. Micromech. Microeng. 23, 015009.

Dong, K., Wu, Z.Y., Deng, J.N., Wang, A.C., Zou, H.Y., Chen, C.Y., Hu, D.M., Gu, B.H., Sun, B.Z., Wang, Z.L., 2018. A stretchable yarn embedded triboelectric nanogenerator as electronic skin for biomechanical energy harvesting and multifunctional pressure sensing. Adv. Mater. 30, 1804944.

Fan, Z.C., Hwang, K.C., Rogers, J.A., Huang, Y., Zhang, Y.H., 2018. A double perturbation method of postbuckling analysis in 2D curved beams for assembly of 3D ribbon-shaped structures. J. Mech. Phys. Solids 111, 215–238.

Fu, H.R., Nan, K.W., Bai, W.B., Huang, W., Bai, K., Lu, L.Y., Zhou, C.Q., Liu, Y.P., Liu, F., Wang, J.T., Han, M.D., Yan, Z., Luan, H.W., Zhang, Y.J., Zhang, Y.T., Zhao, J. N., Cheng, X., Li, M.Y., Lee, J.W., Liu, Y., Fang, D.N., Li, X.L., Huang, Y., Zhang, Y.H., Rogers, J.A., 2018. Morphable 3D mesostructures and microelectronic devices by multistable buckling mechanics. Nat. Mater. 17, 268–276.

Gao, Y.J., Ota, H., Schaler, E.W., Chen, K., Zhao, A., Gao, W., Fahad, H.M., Leng, Y.G., Zheng, A.Z., Xiong, F.R., Zhang, C.C., Tai, L.C., Zhao, P.D., Fearing, R.S., Javey, A., 2017. Wearable microfluidic diaphragm pressure sensor for health and tactile touch monitoring. Adv. Mater. 29, 1701985.

Ge, J., Sun, L., Zhang, F.R., Zhang, Y., Shi, L.A., Zhao, H.Y., Zhu, H.W., Jiang, H.L., Yu, S.H., 2016. A stretchable electronic fabric artificial skin with pressure-, lateral strain-, and flexion-sensitive properties. Adv. Mater. 28, 722–728.

Gong, S., Schwalb, W., Wang, Y.W., Chen, Y., Tang, Y., Si, J., Shirinzadeh, B., Cheng, W.L., 2014. A wearable and highly sensitive pressure sensor with ultrathin gold nanowires. Nat. Commun. 5, 3132.
Ha, M., Lim, S., Cho, S., Lee, Y., Na, S., Baig, C., Ko, H., 2018. Skin-inspired hierarchical polymer architectures with gradient stiffness for spacer-free, ultrathin, and highly sensitive triboelectric sensors. ACS Nano 12, 3964–3974.
Ha, T., Tran, J., Liu, S.Y., Jang, H., Jeong, H., Mitbander, R., Huh, H., Qiu, Y.T., Duong, J., Wang, R.L., Wang, P.L., Tandon, A., Sirohi, J., Lu, N.S., 2019. A chest-laminated ultrathin and stretchable E-tattoo for the measurement of electrocardiogram, seismocardiogram, and cardiac time intervals. Adv. Sci. 6, 1900290.
Han, M.D., Wang, H.L., Yang, Y., Liang, C.M., Bai, W.B., Yan, Z., Li, H.B., Xue, Y.G., Wang, X.L., Akar, B., Zhao, H.B., Luan, H.W., Lim, J., Kandela, I., Ameer, G.A., Zhang, Y.H., Huang, Y., Rogers, J.A., 2019. Three-dimensional piezoelectric polymer microsystems for vibrational energy harvesting, robotic interfaces and biomedical implants. Nat. Electron. 2, 26–35.
Heyneman, B., Cutkosky, M.R., 2016. Slip classification for dynamic tactile array sensors. Int. J. Robot. Res. 35, 404–421.
Hong, S.Y., Lee, Y.H., Park, H., Jin, S.W., Jeong, Y.R., Yun, J., You, I., Zi, G., Ha, J.S., 2016. Stretchable active matrix temperature sensor array of polyaniline nanofibers for electronic skin. Adv. Mater. 28, 930–935.
Hu, C.F., Su, W.S., Fang, W., 2011. Development of patterned carbon nanotubes on a 3D polymer substrate for the flexible tactile sensor application. J. Micromech. Microeng. 21, 115012.
Huang, Z.Y., Hong, W., Suo, Z.G., 2005. Nonlinear analyses of wrinkles in a film bonded to a compliant substrate. J. Mech. Phys. Solids. 53, 2101–2118.
Jang, K.-I., Chung, H.U., Xu, S., Lee, C.H., Luan, H.W., Jeong, J., Cheng, H.Y., Kim, G.-T., Han, S.Y., Lee, J.W., Kim, J., Cho, M., Miao, F.X., Yang, Y.Y., Jung, H.N., Flavin, M., Liu, H., Kong, G.W., Yu, K.J., Rhee, S.I., Chung, J., Kim, B., Kwak, J.W., Yun, M.H., Kim, J.Y., Song, Y.M., Paik, U., Zhang, Y.H., Huang, Y., Rogers, J.A., 2015. Soft network composite materials with deterministic and bio-inspired designs. Nat. Commun. 6, 6566.
Jeong, H., Wang, L., Ha, T., Mitbander, R., Yang, X.X., Dai, Z.H., Qiao, S.T., Shen, L.X., Sun, N., Lu, N.S., 2019. Modular and reconfigurable wireless E-tattoos for personalized sensing. Adv. Mater. Technol. 4, 1900117.
Jiang, H.Q., Khang, D.-Y., Song, J.Z., Sun, Y.G., Huang, Y., Rogers, J.A., 2007a. Finite deformation mechanics in buckled thin films on compliant supports. Proc. Natl. Acad. Sci. U.S.A. 104, 15607–15612.
Jiang, H.Q., Sun, Y.G., Rogers, J.A., Huang, Y., 2007b. Mechanics of precisely controlled thin film buckling on elastomeric substrate. Appl. Phys. Lett. 90, 133119.
Jiang, H.Q., Sun, Y.G., Rogers, J.A., Huang, Y., 2008. Post-buckling analysis for the precisely controlled buckling of thin film encapsulated by elastomeric substrates. Int. J. Solids Struct. 45, 2014–2023.
Kane, B.J., Cutkosky, M.R., Kovacs, G.T.A., 2000. A traction stress sensor array for use in high-resolution robotic tactile imaging. J. Microelectromech. S. 9, 425–434.
Kang, D., Pikhitsa, P.V., Choi, Y.W., Lee, C., Shin, S.S., Piao, L., Park, B., Suh, K.Y., Kim, T., Choi, M., 2014. Ultrasensitive mechanical crack-based sensor inspired by the spider sensory system. Nature 516, 222–226.
Kim, D.H., Liu, Z.J., Kim, Y.-S., Wu, J., Song, J.Z., Kim, H.S., Huang, Y., Hwang, K.C., Zhang, Y.W., Rogers, J.A., 2009. Optimized structural designs for stretchable silicon integrated circuits. Small 5, 2841–2847.
Kim, H.J., Sim, K., Thukral, A., Yu, C.J., 2017. Rubbery electronics and sensors from intrinsically stretchable elastomeric composites of semiconductors and conductors. Sci. Adv. 3, e1701114.
Kim, J., Lee, M., Shim, H.J., Ghaffari, R., Cho, H.R., Son, D., Jung, Y.H., Soh, M., Choi, C., Jung, S., Chu, K., Jeon, D., Lee, S.T., Kim, J.H., Choi, S.H., Hyeon, T., Kim, D.H., 2014. Stretchable silicon nanoribbon electronics for skin prosthesis. Nat. Commun. 5, 5747.
Kim, K.K., Hong, S., Cho, H.M., Lee, J., Suh, Y.D., Ham, J., Ko, S.H., 2015. Highly sensitive and stretchable multidimensional strain sensor with prestrained anisotropic metal nanowire percolation networks. Nano Lett. 15, 5240–5247.
Kim, M.K., Parasuraman, R.N., Wang, L., Park, Y., Kim, B., Lee, S.J., Lu, N.S., Min, B.-C., Lee, C.H., 2019. Soft-packaged sensory glove system for human-like natural interaction and control of prosthetic hands. NPG Asia Mater. 11, 43.
Ko, H.C., Shin, G., Wang, S.D., Stoykovich, M.P., Lee, J.W., Kim, D.H., Ha, J.S., Huang, Y., Hwang, K.C., Rogers, J.A., 2009. Curvilinear electronics formed using silicon membrane circuits and elastomeric transfer elements. Small 5, 2703–2709.
Landau, L.D., Lifshitz, E.M., 1959. Theory of Elasticity. Pergamon, London.
Lee, H., Chung, J., Chang, S., Yoon, E., 2008. Normal and shear force measurement using a flexible polymer tactile sensor with embedded multiple capacitors. J. Microelectromech. S. 17, 934–942.
Lee, S., Kim, J., Yun, I., Bae, G.Y., Kim, D., Park, S., Yi, I.M., Moon, W., Chung, Y., Cho, K., 2019a. An ultrathin conformable vibration-responsive electronic skin for quantitative vocal recognition. Nat. Commun. 10, 2468.
Lee, Y., Park, J., Choe, A., Cho, S., Kim, J., Ko, H., 2019b. Mimicking human and biological skins for multifunctional skin electronics. Adv. Funct. Mater. 30, 1904523.
Li, K., Cheng, X., Zhu, F., Li, L.Z., Xie, Z.Q., Luan, H.W., Wang, Z.H., Ji, Z.Y., Wang, H.L., Liu, F., Xue, Y.G., Jiang, C.Q., Feng, X., Li, L.M., Rogers, J.A., Huang, Y., Zhang, Y.H., 2019a. A generic soft encapsulation strategy for stretchable electronics. Adv. Funct. Mater. 29, 1806630.
Li, S.P., Han, M.D., Rogers, J.A., Zhang, Y.H., Huang, Y., Wang, H.L., 2019b. Mechanics of buckled serpentine structures formed via mechanics-guided, deterministic three-dimensional assembly. J. Mech. Phys. Solids 125, 736–748.
Lin, L., Xie, Y.N., Wang, S.H., Wu, W.Z., Niu, S.M., Wen, X.N., Wang, Z.L., 2013. Triboelectric active sensor array for self-powered static and dynamic pressure detection and tactile imaging. ACS Nano 7, 8266–8274.
Lipomi, D.J., Vosgueritchian, M., Tee, B.C.K., Hellstrom, S.L., Lee, J.A., Fox, C.H., Bao, Z.N., 2011. Skin-like pressure and strain sensors based on transparent elastic films of carbon nanotubes. Nat. Nanotechnol. 6, 788–792.
Liu, Y., Pharr, M., Salvatore, G.A., 2017. Lab-on-skin: a review of flexible and stretchable electronics for wearable health monitoring. ACS Nano 11, 9614–9635.
Liu, Y., Wang, X.J., Xu, Y.M., Xue, Z.G., Zhang, Y., Ning, X., Cheng, X., Xue, Y.G., Lu, D., Zhang, Q.H., Zhang, F., Liu, J.X., Guo, X.G., Hwang, K.C., Huang, Y., Rogers, J.A., Zhang, Y.H., 2019a. Harnessing the interface mechanics of hard films and soft substrates for 3D assembly by controlled buckling. Proc. Natl. Acad. Sci. USA 116, 15368–15377.
Liu, Y., Xu, Z., Hwang, K.C., Huang, Y., Zhang, Y.H., 2019b. Postbuckling analyses of frame mesostructures consisting of straight ribbons for mechanically guided three-dimensional assembly. P. Roy. Soc. A-Math. Phy. 475, 20190012.
Lu, N.S., Lu, C., Yang, S.X., Rogers, J., 2012. Highly sensitive skin-mountable strain gauges based entirely on elastomers. Adv. Funct. Mater. 22, 4044–4050.
Luo, G.Q., Fu, H.R., Cheng, X., Bai, K., Shi, L.P., He, X.D., Rogers, J.A., Huang, Y., Zhang, Y.H., 2019. Mechanics of bistable cross-shaped structures through loading-path controlled 3D assembly. J. Mech. Phys. Solids 129, 261–277.
Ma, C.W., Hsu, L.S., Kuo, J.C., Yang, Y.J., 2015. A flexible tactile and shear sensing array fabricated using a novel buckypaper patterning technique. Sens. Actuator A-Phys. 231, 21–27.
Ma, Q., Cheng, H., Jang, K.-I., Luan, H., Hwang, K.-C., Rogers, J.A., Huang, Y., Zhang, Y., 2016. A nonlinear mechanics model of bio-inspired hierarchical lattice materials consisting of horseshoe microstructures. J. Mech. Phys. Solids 90, 179–202.
Ma, Q., Zhang, Y.H., 2016. Mechanics of fractal-inspired horseshoe microstructures for applications in stretchable electronics. J. Appl. Mech. 83, 111008.
Ma, Y.J., Choi, J., Hourlier-Fargette, A., Xue, Y.G., Chung, H.U., Lee, J.Y., Wang, X.F., Xie, Z.Q., Kang, D., Wang, H.L., Han, S., Kang, S.K., Kang, Y., Yu, X., Slepian, M.J., Raj, M.S., Model, J.B., Feng, X., Ghaffari, R., Rogers, J.A., Huang, Y., 2018. Relation between blood pressure and pulse wave velocity for human arteries. Proc. Natl. Acad. Sci. USA 115, 11144–11149.
Ma, Y.J., Zhang, Y.C., Cai, S.S., Han, Z.Y., Liu, X., Wang, F.L., Cao, Y., Wang, Z.H., Li, H.F., Chen, Y.H., Feng, X., 2020. Flexible hybrid electronics for digital healthcare. Adv. Mater. 32, 1902062.
Mannsfeld, S.C.B., Tee, B.C.K., Stoltenberg, R.M., Chen, C.V.H.H., Barman, S., Muir, B.V.O., Sokolov, A.N., Reese, C., Bao, Z.N., 2010. Highly sensitive flexible pressure sensors with microstructured rubber dielectric layers. Nat. Mater. 9, 859–864.
Mu, C.H., Song, Y.Q., Huang, W.T., Ran, A., Sun, R.J., Xie, W.H., Zhang, H.W., 2018. Flexible normal-tangential force sensor with opposite resistance responding for highly sensitive artificial skin. Adv. Funct. Mater. 28, 1707503.

Ning, X., Wang, H.L., Yu, X.G., Soares, J.A.N.T., Yan, Z., Nan, K.W., Velarde, G., Xue, Y.G., Sun, R.J., Dong, Q.Y., Luan, H.W., Lee, C.M., Chempakasseril, A., Han, M. D., Wang, Y.Q., Li, L.M., Huang, Y., Zhang, Y.H., Rogers, J.A., 2017. 3D tunable, multiscale, and multistable vibrational micro-platforms assembled by compressive buckling. Adv. Funct. Mater. 27, 1605914.

Ning, X., Yu, X.G., Wang, H.L., Sun, R.J., Corman, R.E., Li, H.B., Lee, C.M., Xue, Y.G., Chempakasseril, A., Yao, Y., Zhang, Z.Q., Luan, H.W., Wang, Z.Z., Xia, W., Feng, X., Ewoldt, R.H., Huang, Y., Zhang, Y.H., Rogers, J.A., 2018. Mechanically active materials in three-dimensional mesostructures. Sci. Adv. 4, eaat8313.

Ohka, M., Kobayashi, H., Mitsuya, Y., 2005. Sensing characteristics of an optical three-axis tactile sensor mounted on a multi-fingered robotic hand. In: 2005 IEEE/RSJ International Conference on Intelligent Robots and Systems. Edmonton, pp. 493–498.

Pan, T.S, Pharr, M., Ma, Y.J., Ning, R., Yan, Z., Xu, R.X., Feng, X., Huang, Y., Rogers, J.A., 2017. Experimental and theoretical studies of serpentine interconnects on ultrathin elastomers for stretchable electronics. Adv. Funct. Mater. 27, 1702589.

Pang, C., Lee, G.Y., Kim, T., Kim, S.M., Kim, H.N., Ahn, S.H., Suh, K.Y., 2012. A flexible and highly sensitive strain-gauge sensor using reversible interlocking of nanofibres. Nat. Mater. 11, 795–801.

Park, J., Kim, J., Hong, J., Lee, H., Lee, Y., Cho, S., Kim, S.W., Kim, J.J., Kim, S.Y., Ko, H., 2018. Tailoring force sensitivity and selectivity by microstructure engineering of multidirectional electronic skins. NPG Asia Mater. 10, 163–176.

Park, J., Kim, M., Lee, Y., Lee, H.S., Ko, H., 2015. Fingertip skin–inspired microstructured ferroelectric skins discriminate static/dynamic pressure and temperature stimuli. Sci. Adv. 1, e1500661.

Park, J., Lee, Y., Hong, J., Ha, M., Jung, Y.D., Lim, H., Kim, S.Y., Ko, H., 2014a. Giant tunneling piezoresistance of composite elastomers with interlocked microdome arrays for ultrasensitive and multimodal electronic skins. ACS Nano 8, 4689–4697.

Park, J., Lee, Y., Hong, J., Lee, Y., Ha, M., Jung, Y., Lim, H., Kim, S.Y., Ko, H., 2014b. Tactile-direction-sensitive and stretchable electronic skins based on human-skin-inspired interlocked microstructures. ACS Nano 8, 12020–12029.

Park, S., Kim, H., Vosgueritchian, M., Cheon, S., Kim, H., Koo, J.H., Kim, T.R., Lee, S., Schwartz, G., Chang, H., Bao, Z.N., 2014c. Stretchable energy-harvesting tactile electronic skin capable of differentiating multiple mechanical stimuli modes. Adv. Mater. 26, 7324–7332.

Rogers, J.A., Someya, T., Huang, Y., 2010. Materials and mechanics for stretchable electronics. Science 327, 1603–1607.

Scheibert, J., Leurent, S., Prevost, A., Debrégeas, G., 2009. The role of fingerprints in the coding of tactile information probed with a biomimetic sensor. Science 323, 1503–1506.

Shi, Y., Pei, P.Y., Cheng, X., Yan, Z., Han, M.D., Li, Z., Gao, C.F., Rogers, J.A., Huang, Y., Zhang, Y.H., 2018. An analytic model of two-level compressive buckling with applications in the assembly of free-standing 3D mesostructures. Soft Matter. 14, 8828–8837.

Someya, T., Bao, Z., Malliaras, G.G., 2016. The rise of plastic bioelectronics. Nature 540, 379–385.

Song, J.Z., Huang, Y., Xiao, J.L., Wang, S.D., Hwang, K.C., Ko, H.C., Kim, D.H., Stoykovich, M.P., Rogers, J.A., 2009. Mechanics of noncoplanar mesh design for stretchable electronic circuits. J. Appl. Phys. 105, 123516.

Su, Y.W., Wu, J., Fan, Z.C., Hwang, K.C., Song, J.Z., Huang, Y., Rogers, J.A., 2012. Postbuckling analysis and its application to stretchable electronics. J. Mech. Phys. Solids 60, 487–508.

Sun, J.Y., Keplinger, C., Whitesides, G.M., Suo, Z.G., 2014. Ionic skin. Adv. Mater. 26, 7608–7614.

Sun, Y.G., Choi, W.M., Jiang, H.Q., Huang, Y., Rogers, J.A., 2006. Controlled buckling of semiconductor nanoribbons for stretchable electronics. Nat. Nanotechnol. 1, 201.

Takei, K., Takahashi, T., Ho, J.C., Ko, H., Gillies, A.G., Leu, P.W., Fearing, R.S., Javey, A., 2010. Nanowire active-matrix circuitry for low-voltage macroscale artificial skin. Nat. Mater. 9, 821–826.

Ting, Y., Suprapto, Nugraha, A., Chiu, C.W., Gunawan, H., 2016. Design and characterization of one-layer PVDF thin film for a 3D force sensor. Sens. Actuator A-Phys. 250, 129–137.

Tomo, T.P., Somlor, S., Schmitz, A., Jamone, L., Huang, W., Kristanto, H., Sugano, S., 2016. Design and characterization of a three-axis hall effect-based soft skin sensor. Sensors 16, 491.

Viry, L., Levi, A., Totaro, M., Mondini, A., Mattoli, V., Mazzolai, B., Beccai, L., 2014. Flexible three-axial force sensor for soft and highly sensitive artificial touch. Adv. Mater. 26, 2659–2664.

Vogt, D.M., Park, Y., Wood, R.J., 2013. Design and characterization of a soft multi-axis force sensor using embedded microfluidic channels. IEEE Sens. J. 13, 4056–4064.

Wang, C.Y., Li, X., Gao, E.L., Jian, M.Q., Xia, K.L., Wang, Q., Xu, Z.P., Ren, T.L., Zhang, Y.Y., 2016a. Carbonized silk fabric for ultrastretchable, highly sensitive, and wearable strain sensors. Adv. Mater. 28, 6640–6648.

Wang, H.B., De Boer, G., Kow, J., Alazmani, A., Ghajari, M., Hewson, R., Culmer, P., 2016b. Design methodology for magnetic field-based soft tri-axis tactile sensors. Sensors 16, 1356.

Wang, L., Beebe, D.J., 2000. A silicon-based shear force sensor: development and characterization. Sens. Actuator A-Phys. 84, 33–44.

Wang, S.D., Xiao, J.L., Song, J.Z., Ko, H.C., Hwang, K.C., Huang, Y., Rogers, J.A., 2010. Mechanics of curvilinear electronics. Soft Matter. 6, 5757–5763.

Won, S.M., Wang, H.L., Kim, B.H., Lee, K., Jang, H., Kwon, K., Han, M.D., Crawford, K.E., Li, H.B., Lee, Y., Yuan, X.B., Kim, S.B., Oh, Y.S., Jang, W.J., Lee, J.Y., Han, S., Kim, J., Wang, X.J., Xie, Z.Q., Zhang, Y.H., Huang, Y., Rogers, J.A., 2019. Multimodal sensing with a three-dimensional piezoresistive structure. ACS Nano 13, 10972–10979.

Wu, J., Liu, Z.J., Song, J.Z., Huang, Y., Hwang, K.C., Zhang, Y.W., Rogers, J.A., 2011. Stretchability of encapsulated electronics. Appl. Phys. Lett. 99, 061911.

Wu, Y.Z., Liu, Y.W., Zhou, Y.L., Man, Q.K., Hu, C., Asghar, W., Li, F.L., Yu, Z., Shang, J., Liu, G., Liao, M.Y., Li, R.W., 2018. A skin-inspired tactile sensor for smart prosthetics. Sci. Robot. 3, eaat0429.

Xie, Z.Q., Avila, R., Huang, Y., Rogers, J.A., 2020. Flexible and stretchable antennas for biointegrated electronics. Adv. Mater. 32, 1902767.

Xu, S., Yan, Z., Jang, K.I., Huang, W., Fu, H., Kim, J., Wei, Z., Flavin, M., McCracken, J., Wang, R., Badea, A., Liu, Y., Xiao, D., Zhou, G., Lee, J., Chung, H.U., Cheng, H., Ren, W., Banks, A., Li, X., Paik, U., Nuzzo, R.G., Huang, Y., Zhang, Y., Rogers, J.A., 2015. Assembly of micro/nanomaterials into complex, three-dimensional architectures by compressive buckling. Science 347, 154–159.

Xue, Z.G., Song, H.L., Rogers, J.A., Zhang, Y.H., Huang, Y., 2018. Mechanically-guided structural designs in stretchable inorganic electronics. Adv. Mater., 1902254

Yan, Z., Zhang, F., Liu, F., Han, M.D., Ou, D.P., Liu, Y.H., Lin, Q., Guo, X.L., Fu, H.R., Xie, Z.Q., Gao, M.Y., Huang, Y.M., Kim, J., Qiu, Y.T., Nan, K.W., Kim, J., Gutruf, P., Luo, H.Y., Zhao, A., Hwang, K.C., Huang, Y., Zhang, Y.H., Rogers, J.A., 2016. Mechanical assembly of complex, 3D mesostructures from releasable multilayers of advanced materials. Sci. Adv. 2, e1601014.

Yang, J.Y., Li, X.P., Lü, X.Z., Bao, W.M., Chen, R.J., 2018. Three-dimensional interfacial stress sensor based on graphene foam. IEEE Sens. J. 18, 7956–7963.

Yang, J.C., Mun, J., Kwon, S.Y., Park, S., Bao, Z.N., Park, S., 2019. Electronic skin: recent progress and future prospects for skin-attachable devices for health monitoring, robotics, and prosthetics. Adv. Mater. 31, 1904765.

Yao, S., Swetha, P., Zhu, Y., 2018. Nanomaterial-enabled wearable sensors for healthcare. Adv. Healthc. Mater. 7, 1700889.

Yao, S., Zhu, Y., 2014. Wearable multifunctional sensors using printed stretchable conductors made of silver nanowires. Nanoscale 6, 2345–2352.

Yousef, H., Boukallel, M., Althoefer, K., 2011. Tactile sensing for dexterous in-hand manipulation in robotics—a review. Sens. Actuator A-Phys. 167, 171–187.

Yu, P., Liu, W.T., Gu, C.X., Cheng, X.Y., Fu, X., 2016. Flexible piezoelectric tactile sensor array for dynamic three-axis force measurement. Sensors 16, 819.

Yu, X.G., Xie, Z.Q., Yu, Y., Lee, J., Vazquez-Guardado, A., Luan, H.W., Ruban, J., Ning, X., Akhtar, A., Li, D.F., Ji, B.W., Liu, Y.M., Sun, R.J., Cao, J.Y., Huo, Q.Z., Zhong, Y.S., Lee, C., Kim, S., Gutruf, P., Zhang, C.X., Xue, Y.G., Guo, Q.L., Chempakasseril, A., Tian, P.L., Lu, W., Jeong, J., Yu, Y., Cornman, J., Tan, C., Kim, B., Lee, K., Feng, X., Huang, Y., Rogers, J.A., 2019. Skin-integrated wireless haptic interfaces for virtual and augmented reality. Nature 575, 473–479.

Zhang, F., Fan, Z.C., Zhang, Y.H., 2018. A theoretical model of postbuckling in straight ribbons with engineered thickness distributions for three-dimensional assembly. Int. J. Solids Struct. 147, 254–271.

Zhang, F.J., Zang, Y.P., Huang, D.Z., Di, C, Zhu, D.B., 2015a. Flexible and self-powered temperature–pressure dual-parameter sensors using microstructure-frame-supported organic thermoelectric materials. Nat. Commun. 6, 8356.

Zhang, Y.H., Yan, Z., Nan, K.W., Xiao, D.Q., Liu, Y.H., Luan, H.W., Fu, H.R., Wang, X.Z., Yang, Q.L., Wang, J.C., Ren, W., Si, H.Z., Liu, F., Yang, L.H., Li, H.J., Wang, J. T., Guo, X.L., Luo, H.Y., Wang, L., Huang, Y., Rogers, J.A., 2015b. A mechanically driven form of Kirigami as a route to 3D mesostructures in micro/ nanomembranes. Proc. Natl. Acad. Sci. USA 112, 11757–11764.

Zhu, F., Xiao, H.B., Li, H.B., Huang, Y., Ma, Y.J., 2019. Irregular hexagonal cellular substrate for stretchable electronics. J. Appl. Mech. 86, 034501.